PSFC/RR-08-12

Magnetics R&D – Task D&T-01

MIT Cooperative Agreement
Final Report For FY2008

July 28, 2008

J.V. Minervini, M. Takayasu, J.H. Schultz, J. Feng, A. Radovinsky, L. Chiesa, S. Mahar, M. Salvetti

TABLE OF CONTENTS

Magnetics R&D – Task D&T-01

MIT Cooperative Agreement
Final Report For FY2008

Principal Investigator:	Co-Principal Investigator:
Joseph V. Minervini MIT Plasma Science and Fusion Center NW22-129 Cambridge, MA 02139 Tel: (617) 253-5503 Fax: (617) 253-0807 minervini@psfc.mit.edu	Makoto Takayasu MIT Plasma Science and Fusion Center NW22-109 Cambridge, MA 02139 Tel: (617) 253-8358 Fax: (617) 253-0807 takayasu@psfc.mit.edu

1 PROJECT SUMMARY

The Fusion Technology and Engineering Division (FTED) of the MIT Plasma Science and Fusion Center (PSFC) is nearing the end of the first year of a five year cooperative agreement to carry out a research program aimed at advancing the state of the art and development of magnet technology for fusion applications. This work is being carried out under funding from the Enabling Magnet Technology Program of the Virtual Laboratory for Technology (VLT). The Project is lead by Dr. Joseph V. Minervini (PI) and Dr. Makoto Takayasu (Co-PI). The work is being out in the research laboratories of the MIT Plasma Science and Fusion Center.

The objective of the program is to perform basic research in superconductor and magnet technology which provides understanding of present state-of-the-art superconductors and magnet systems, with the ultimate goal of advancing these technologies for use in future magnetic confinement fusion devices. In previous years this work was oriented towards R&D associated with ITER Magnets, but after the US ITER program was formalized into an official national project under the auspices of the US ITER Project Office (USIPO) the focus of the D&T-01 tasks was shifted to basic studies of magnet technology issues. Although these results can sometimes be directly applied to ITER magnet and conductor applications they are primarily oriented towards magnet technologies anticipated to be used in fusion applications in addition to, or beyond ITER.

The studies performed here are intrinsically fundamental in nature, or in a very early technology development stage. We have selected technical topics which are well suited for study by an academic institution, but the solutions are always approached with a practical experience background of implementing new technology in working devices, and with an eye on eventual technology transfer to industry.

The work reported here is primarily structured around the thesis topic work of our 3 present graduate students. These include Luisa Chiesa (cable transverse stress studies), Matteo Salvetti (fundamental analysis of strain effects in filaments), and Scott Mahar (development of a fiber-optic temperature and strain diagnostic). Chiesa and Mahar will finish their studies by early in the Fall 2008-2009 term and Matteo is expected to finish by Spring Term in 2009.

The program is divided into 6 subtasks:

1. ***Experimental Study of Strain Effects on Superconducting Strands***
2. ***Theoretical Study of Strain Effects on Critical Parameters of Superconducting Filaments and Strands***
3. ***Experimental Study of Transverse Stress Effects on Superconducting Cables***
4. ***Development of an Optical Fiber Diagnostic for Measurement of Temperature and Strain in Superconductor Windings***
5. ***Development of High Temperature Superconducting Magnets for Fusion***
6. ***VLT Enabling Technology Magnets Program Leadership***

2 SUBTASK-1: EXPERIMENTAL STUDY OF STRAIN EFFECTS ON SUPERCONDUCTING STRANDS

2.1 Introduction

Bending effects on Nb_3Sn wires have been investigated to understand the critical current degradation of large Nb_3Sn superconducting cables, such as the ITER conductors. In FY08 characterizations of the critical currents of various Nb_3Sn wires were carried out by a previously reported variable pure-bending strand test device using the 20 T, 195 mm Bitter magnet at the National High Magnetic Field Laboratory (NHMFL). The critical currents were measured over a large range of bending, up to 0.8% of the nominal bending strain at the wire surface. Irreversible degradation of the critical currents due to bending was also evaluated after straightening the wire. Five different Nb_3Sn wires, developed by the ITER parties, were tested. Three of them were internal-tin wires of recent ITER TF US Oxford and Luvata wires and older European (EU) EM-LMI wire, while two of them were a recent EU EAS and an older Furukawa bronze wire. The relations of the measured pure-bending critical currents to the existing uniaxial strain data of the wires are discussed. The experimental data were evaluated with a newly developed integrated model that accounts for neutral axis shift, current transfer length, mechanical filament breakage and uniaxial strain release due to applying bending. The test results of the five wires can be well understood by including these phenomena, however further studies of mechanical properties of superconducting wires under pure bending are recommended.

2.2 Test Method

The bending tests were carried out using our variable bending test device developed and described earlier[1,2,3]. The device can apply a large range of bending, in liquid helium, to a

[1] D.L. Harris, A.A Allegritti, M. Takayasu, and J.V. Minervini, "Pure bending strand test of high performance Nb3Sn wires," Adv. Cryo. Eng., 54, Plenum, N.Y., 341-348, 2008.

[2] D.L. Harris, "Characterization of Nb3Sn superconducting strand under pure bending," MIT Mechanical Engineering Masters Thesis, 2005.

[3] A. Allegritti, "Development and experimental test of a device for the measurements of the critical current of superconducting strands under pure bending conditions," University of Bologna, Department of Mechanical Engineering, Italy, 2006.

strand sample of about 100 mm length, up to 0.8% of the nominal bending strain at the surface of a wire with 0.8 mm diameter. The sample holders are shown in **Fig. 2.1**. Grooved slots for the sample mounting are located at the top and bottom edges of each plate of the sample holder. The plate is made from Ti-6Al-4V plate with dimensions 1" x 6.5" x 0.063". In this way the sample holder locates the neutral plain of the wire to apply pure bending to the samples. Two copper terminators are mounted at each end of the sample holder beam. Both ends of the test sample, 25 mm long, were soldered to the copper terminators on the beam after heat treatment. Each sample had a pair of voltage taps. The voltage tap separation was 50 mm and the distance between a voltage tap and the copper terminator was 25 mm. **Fig. 2.2** shows a sample holder assembly of two beams mounted on beam clamps. A current lead was soldered on each copper terminator. The sample holder beams were deformed to a true circular arc by rotational motions of the beam clamps to apply pure bending to the samples. The clamps were rotated by accessing gears with a rotating shaft from the top flange of the probe dewar. The shaft was driven by a ½ horsepower motor. All tests were performed using the 20 T, 195 mm Bitter magnet at NHMFL, Florida State University.

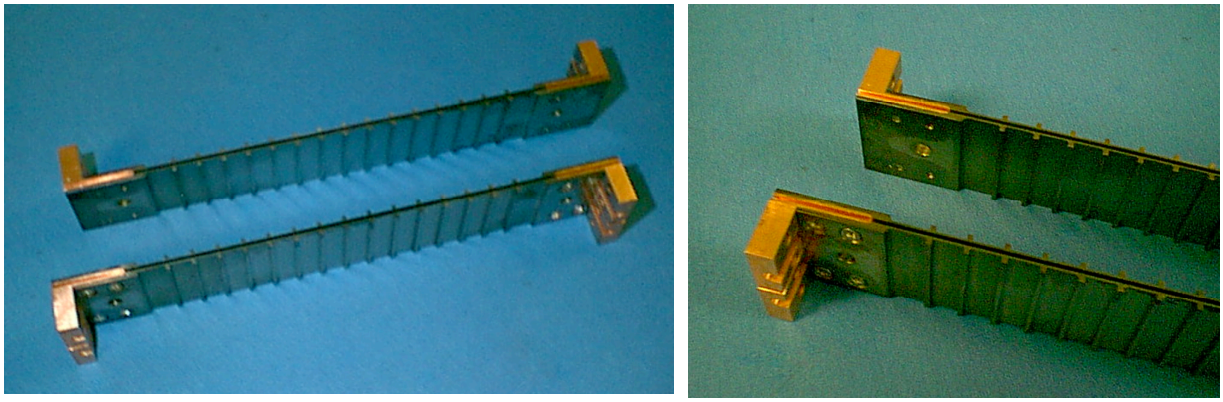

(a) (b)

Fig. 2.1 (a) Pure bending sample holders with copper terminators, which are enlarged in (b).

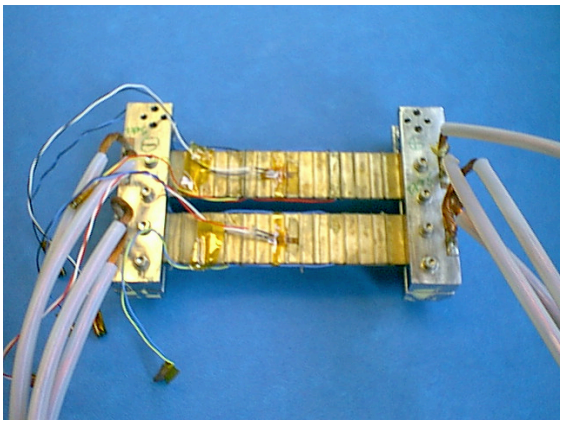

Fig. 2.2 Sample assembly of two beams of the pure bending sample holder on the beam clamps with current leads and strain gauges.

2.3 Experimental Results

We tested five different Nb_3Sn wires which were developed by the ITER parties. Three were internal-tin wires of recently developed ITER TF US Oxford and Luvata wires and EU EM-LMI wire. Two of them were bronze wires of EU EAS and Japanese Furukawa designs.

The bending strain values mentioned above, for example 0.8%, are so called nominal values of the maximum bending strain at the wire surface. The actual peak bending strain of the filaments of the tested wires was about 67% of the nominal bending strain values (0.8% nominal bending is corresponding to about 0.54% peak filament bending.). The ratio of the peak bending strain to the nominal bending strain depends on the Cu:non-Cu ration of the wire.

2.3.1 ITER TF pre-production Oxford and Luvata wires

In **Figs. 2.3** (a) and (b) the bending test results of Oxford and Luvata wires at 15 T are plotted as a function of the peak filament bending strains, respectively. As seen in these figures the critical currents degraded with increasing bending strains. At about 0.55% peak filament bending strains the critical currents were degraded by 47% for Oxford wire and 40% for Luvata wire. Interestingly, the critical current of Luvata wire almost recovered, however that of the Oxford wire showed a significant permanent degradation. The irreversible degradations were about 13% for Oxford wire and 1.3% for Luvata wire. It is noted that there is a significant difference of the bending effect between those two wires even if both wires were made of internal tin Nb_3Sn process.

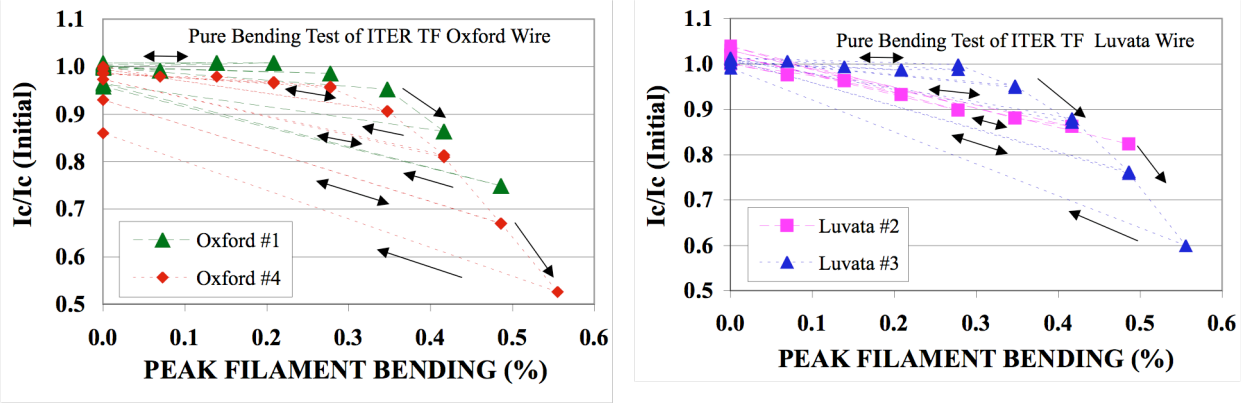

(a) (b)

Fig. 2.3 Normalized critical currents as a function of the peak filament bending strains for (a) Oxford and (b) Luvata wires.

2.3.2 Other ITER related wires

In the second series of the bending test, three wires were tested; one of them is EAS advanced bronze wire developed recently by EU, and others are EM-LMI internal-tin wire and Japanese Furukawa bronze wire, both developed for the ITER model coil program. These wires were tested in the same way as that used for the Oxford and Luvata wires, but the magnetic field strength for the bending tests of these samples was 12 T instead of 15 T,

since there was a magnet problem for 15 T operation. Results of the EAS, EM-LMI and Furukawa wire samples are shown in **Fig. 2.4**.

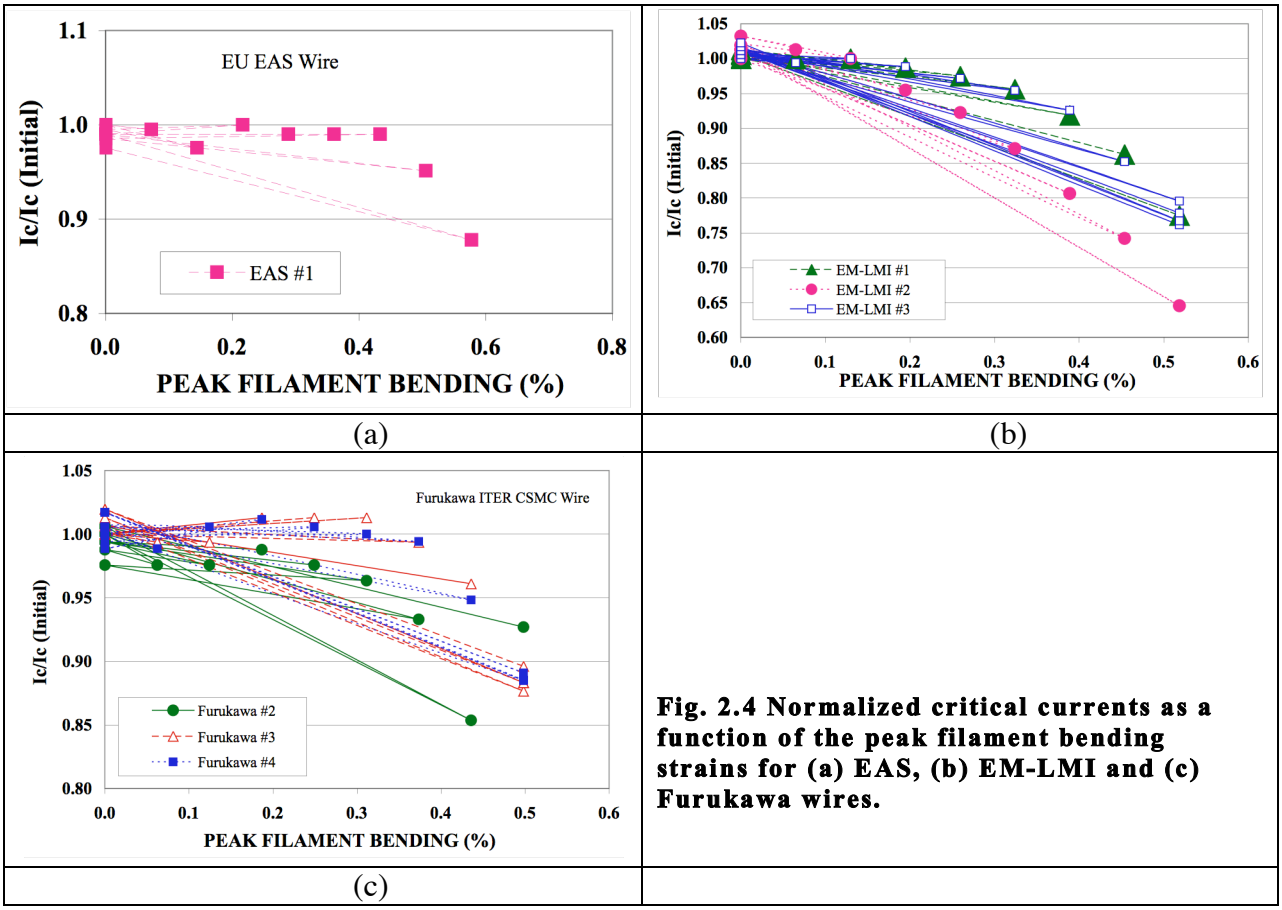

Fig. 2.4 Normalized critical currents as a function of the peak filament bending strains for (a) EAS, (b) EM-LMI and (c) Furukawa wires.

The critical current of the EAS sample degraded by 12 % after 0.58% peak filament bending (0.8% nominal bending). Permanent degradation was about 2%. The critical current of EM-LMI samples degraded by 30% due to the 0.52% peak bending. However, it was noticed for EM-LMI samples that the critical currents at the zero bending strain seemed to increase very gradually after each bending strain cycle. The critical currents of Furukawa samples degraded by 12% due to the 0.50% peak bending. The critical currents of Furukawa samples at the zero bending strain increased gradually after each bending cycle, and also it is noticed for Furukawa samples that the critical currents increased by 1% at the peak bending strains of about 0.3%.

2.4 Model Analysis

The critical current of a multi-filamentary superconducting strand under bending strain has been formulated by Ekin[4]. Ekin considered critical current distributions due to uniaxial strain geometry in twisted filaments of a strand under bending while taking into account the current

[4]J.W. Ekin, "Strain Scaling law and the prediction of uniaxial and bending strain effects in multifilamentary superconductors," in *Filamentary A15 Superconductors*, Proceedings of the tropical conference on A15 superconductors, Ed by M. Suenaga and A. Clark, Plenum Press, New York, 187-203, 1980.

transfer length between filaments with regards to the twist pitch length. Two extreme cases have been considered; long twist pitch (or low inter-filament resistivity), and short twist pitch (or high inter-filament resistivity). We will call the former case "perfect current transfer", and the latter "no current transfer." As shown below the experimental results of the critical currents are well fitted to the prediction of the perfect current transfer model only at small bending rates, and then drop off toward the line of no current transfer model with increasing bending. We have investigated various effects due to mechanical bending, that is, neutral axis shift[4], current transfer length, filament breakage, and uniaxial strain releasing. To analyze the critical current of the bending effects, the scaling formula recommended recently by Bottura[5] was used.

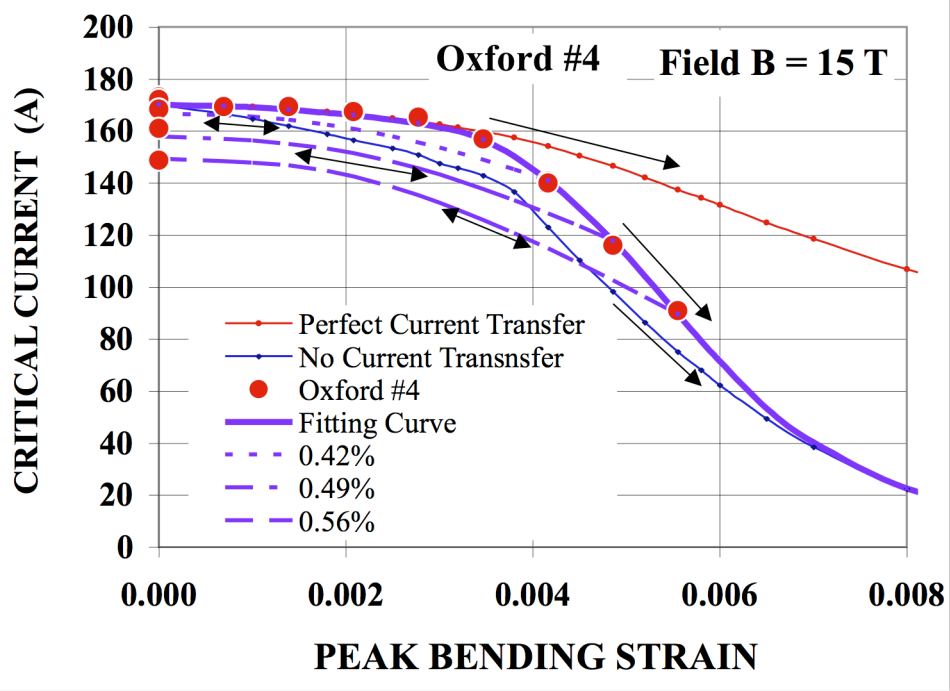

Fig. 2.5 Ic vs. peak bending strain results measured for Oxford wire (red solid circles). Lines are obtained from mode calculations: Fine red and blue lines are for perfect current transfer and no current transfer models, respectively. Measured results fit a thick solid purple line which was obtained from the newly developed model. The dotted lines show recovery curves of the critical currents after the peak bendings of 0.42%, 0.49% and 0.56%. The recovered critical currents at zero bending agree well with the experimental results.

[5] L. Bottura, 2.4.2008, "Jc(B,T,ε) Parameterization for ITER Nb3Sn Production," CERN-ITER collaboration report, Version 2, April 2, 2008.

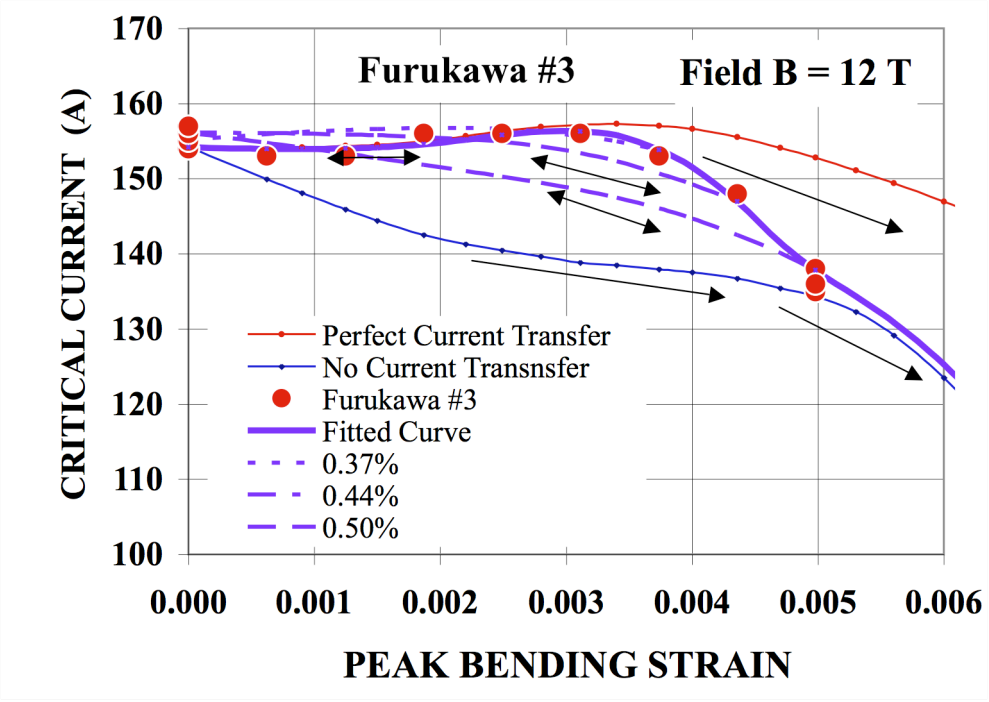

Fig.2.6 Ic vs. peak bending strain results measured for Furukawa wire (red solid circles). Lines are obtained from mode calculations: Fine red and blue lines are for perfect current transfer and no current transfer models, respectively. Measured results fit a solid purple line which was obtained from the newly developed model. The dotted lines show recovery curves of the critical currents after the peak bendings of 0.37%, 0.44% and 0.50%. The maximum of the critical currents at about 0.3% peak bending and also the recovered critical currents at zero bending agree well with the experimental results.

All test results were evaluated with the newly developed model, however two cases of them are given below. **Figs. 2.5** and **2.6** show critical current bending behaviors of Oxford wire and Furukawa wire, respectively. Measured data lie between lines obtained from the perfect current transfer model (red line) and the no current transfer model (blue line). The thick solid purple line was obtained by taking account of the neutral axis shift, current transfer length, filament breakage and uniaxial strain releasing in order to fit the experimental data. The Oxford wire sample showed significant irreversible permanent degradation which could be explained with 2% filament breakage due to tension at 0.56% bending strain. The 1% increase of the critical current for Furukawa wire sample could be explained by a 70 μm shift of the neutral axis.

Bending behaviors of Nb3Sn wires can be well understood by using a newly developed integrated model which accounts for neutral axis shift, current transfer length, mechanical filament breakage and uniaxial strain release. However, further investigations of mechanical properties of superconducting wires under pure bending are recommended.

Acknowledgements
A portion of this work was performed at the National High Magnetic Field Laboratory, Florida State University.

3 SUBTASK-2: THEORETICAL STUDY OF STRAIN EFFECTS ON CRITICAL PARAMETERS OF SUPERCONDUCTING FILAMENTS AND STRANDS

The goal of this research is to understand and model the behavior of the superconducting critical parameters of Aluminum, Niobium, Nb_3Sn and Nb_3Al in the presence of a generic applied strain tensor. Experimental data show that the commonly used power-law descriptions of T_c (ε) and B_{c2}*(ε) break down at applied intrinsic strains exceeding the range –0.5 % < ε < +0.5 %. To our knowledge, no model is available to properly describe the effect of high strain states on the critical parameters of low temperature superconductors. Concurrently, the presence of high longitudinal and bending strains on superconducting magnets is entering a range of clear engineering significance and the source of performance suppression in nuclear fusion, high-energy physics, high field NMR, and cyclotron applications.

Our effort concentrates on the quantitative modeling of strain effects by using ab-initio Density Functional Theory (DFT) codes to calculate the material superconducting critical parameters under generic applied strain conditions. In particular, our study concentrates on the effects of strain stains on the critical superconducting temperature T_c. The study of the strain dependence of the magnetic critical field on a pure microscopic basis is still out of reach. However, the knowledge of the merely T_c dependence on strain would allow a considerable improvement of the available engineering scaling equations, which rely on a T_c dependence on strain fitted from experimental data.

Critical temperature T_c: The critical temperature T_c of low temperature superconducting materials (Al, Nb, Nb_3Sn, Nb_3Al, etc.) is determined by the electron-phonon coupling. The most important parameter regulating the electron-phonon coupling is the electron-phonon coupling constant λ that can be calculated using the theory of electron-phonon interactions developed by Migdal and Eliashberg. Low temperature superconducting materials are characterized by high values of λ, which means that the electrons and the phonons can easily couple to form Cooper pairs[6].

During the past years the use of low temperature superconducting materials such as Nb_3Sn has been advanced to their application under increasingly higher magnetic fields and, as a consequence, higher mechanical loads. Experiments have shown that the critical parameters of the superconductors (T_c, H_{c2}, I_c) deteriorate in presence of an imposed strain tensor. Experimental observations show that the sensitivity of Nb_3Sn to the hydrostatic component of the strain tensor is moderate, while the sensitivity to the deviatoric component (i.e., shear deformations) is more pronounced[7, 8]. Furthermore, not all the low temperature superconducting materials show the same sensitivity to the strain tensor. For instance, Nb_3Sn shows a high sensitivity while Nb_3Al does not.

---

[6] Philip B. Allen, The electron-phonon coupling constant λ^*, Handbook of Superconductivity, Academic Press,NY, 1999, Ch. 9, Sec. G, pp.478-483.

[7] W. Denis Markiewicz, Elastic stiffness model for the critical temperature T_c of Nb_3Sn including strain dependence, Cryogenics 44, pp.767-782, 2004.

[8] W. Denis Markiewicz, Invariant formulation of the strain dependence of the critical temperature T_c of Nb_3Sn in a three term approximation, Cryogenics 44, pp.895-908, 2004.

Part of our current research is focused on modeling the presence of an arbitrary strain state on Aluminum, Niobium, Nb_3Sn and Nb_3Al lattice structures and on the understanding of how the electron-phonon coupling constant λ and the critical temperature T_c are affected by it. In fact, the imposition of a strain state to a crystal lattice modifies both the phonon dispersion curves and the electronic energy bands of the material. These are the two main ingredients needed to calculate the value of the electron-phonon coupling constant λ and they are sensitive to strain, presence of impurities, defects, structural transformations (such as the martensitic transformation experienced by Nb_3Sn), grain boundaries, etc.

Until only a few years ago, computational power seriously limited our capability to investigate this kind of problems given the high computational intensity required to accurately describe the electron-phonon coupling phenomena. Nevertheless, today the introduction of faster computers, the use of cluster-based architectures/supercomputing and the optimization of ab-initio Density Functional Theory codes[9] allow us to extend the modeling of simple "perfect" unit cells describing the superconductor lattice to the modeling of more complex cells featuring the presence of simple defects such as impurities, vacancies or grain boundaries.

We are currently collaborating with the MIT Departments of Mechanical Engineering and Material Science and Engineering with the goal of using an ab-initio DFT code to model the effect of strain on the critical temperature T_c of Aluminum, Niobium, Nb_3Sn and Nb_3Al. Aluminum is superconducting below a temperature of about 1.16 K and it is not an important material for applications in superconductivity. However, it is the material that allows the easiest and fastest benchmarking of our DFT code. Furthermore, Al is one of the elements present in Nb_3Al and the study of its electronic and superconducting properties becomes important in understanding the differences between the superconducting properties of Nb_3Sn and Nb_3Al.

In particular, we are interested in understanding the origin of the different sensitivity to strain shown by Nb_3Sn and Nb_3Al. This could be solely related to the elastic and electronic properties of the materials[10, 11]. The use of an ab-initio DFT code allows us to model the superconducting materials using a bottom-up approach. The simulations we have already carried out for Aluminum, Niobium and Nb_3Al show very good agreement (within 5%) with the experimental data on the phonon dispersion curves, the lattice parameters and the elastic constants of the investigated materials (Table 3.1 and Figs. 3.1-3.3). The only exceptions to such good accuracies emerge in the case of one elastic constant (C_{44}) and one phonon dispersion branch of Niobium because of the presence of a Kohn anomaly[12]. During the past year some of our effort has been directed to the understanding of this behavior and to the

[9] J. Kohanoff and N.I. Gidopoulos, Density Functional Theory: Basics, New Trends and Applications, Handbook of Molecular Physics and Quantum Chemistry, vol. 2, Part 5, Chapter 26, pp.532-568.

[10] Z.W. Lu and Barry M. Klein, Anharmonic Effects in the A15 Compounds Induced by Sublattice Distortions, Phys. Rev. Lett. 79, 1361, 1997.

[11] B. Sadigh and V. Ozolins, Structural instability and electronic excitations in Nb_3Sn, Phys. Rev. B 57, 5 2793, 1998.

[12] W. Kohn, Image of the Fermi surface in the vibration spectrum of a metal, Phys. Rev. Lett. 2, 393, 1959.

calibration of the code in a way to properly capture the effect of the Kohn anomaly. This turned out to be a challenge that also other groups interested in superconductivity are facing[13] recently. Our calculations suggest that a correct calculation of C_{44} requires the extension of the current DFT codes to the use Wannier function formalism[14,15], an optimized interpolation techniques that allows reducing the computational cost of DFT calculations. The group of Professor Marzari at the MIT Material Science and Engineering Department is currently implementing this technique on the code in our use[16]. This will enable us to have a reliable tool to model with confidence the effect of the Niobium lattice distortions on the Niobium critical temperature T_c.

TABLE 3.1

Niobium			
Parameter	Experimental value [Mbar]	Calculated value [Mbar]	Accuracy
Lattice parameter *a*	6.24 au	6.2513 au	0.18%
C_{11}	2.2570	2.41029	4.6%
C_{12}	1.3320	1.37483	3.2%
B_m	1.730	1.71998	0.6%
C_{44}	0.3020	0.21106	32%

[13] P. Aynajian *et al.*, Energy Gaps and Kohn Anomalies in Elemental Superconductors, Science, vol. 319, 1509, 2008.

[14] F. Giustino, M. L. Cohen and S. G. Louie, Phys. Rev. B **76**, 165108, 2007.

[15] J. R. Yates, X. Wang, D. Vanderbilt and I. Souza, Phys. Rev. B **75**, 195121, 2007.

[16] A.A. Mostofi, J.R.Yates, Y.-S. Lee, I. Souza, D. Vanderbilt and N. Marzari Comput. Phys. Commun. **178**, 685, 2008.

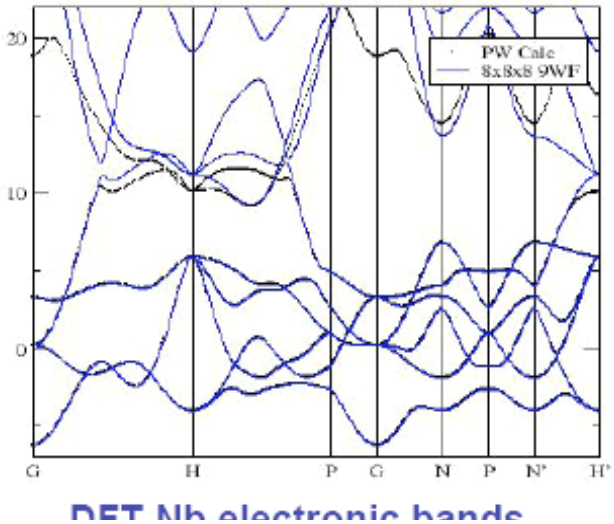

Fig. 3.1 Niobium electronic bands calculated using the standard DFT code (PW) and using the Wannier function formalism (9WF).

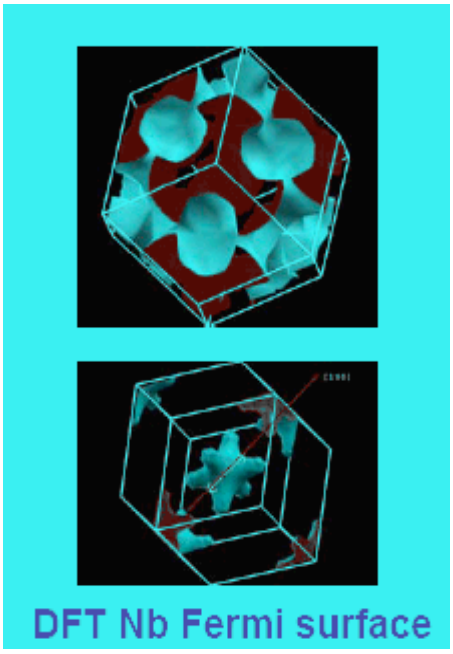

Fig. 3.2 Calculated Fermi surfaces of Niobium.

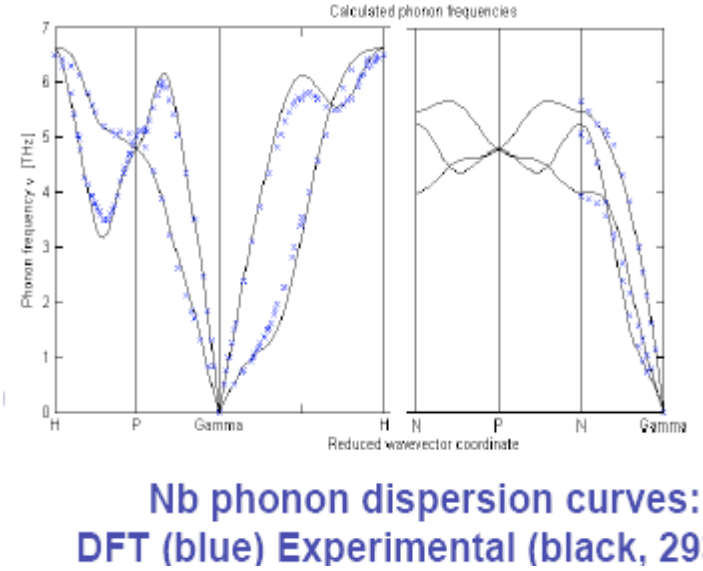

Fig. 3.3 Calculated phonon dispersion curves of Niobium and measured values at 293 K.

During the past year, we have also performed the calculation of the T_c dependence on pressure and simple uniaxial strain for the case of Aluminum. The dependence of T_c on pressure can be directly confronted to the values of T_c measured in experiments on single crystals using diamond anvil cells. We obtain an optimal agreement between the calculated values (obtained using our DFT code and the McMillan equation) and the measured values (Fig. 3.4).

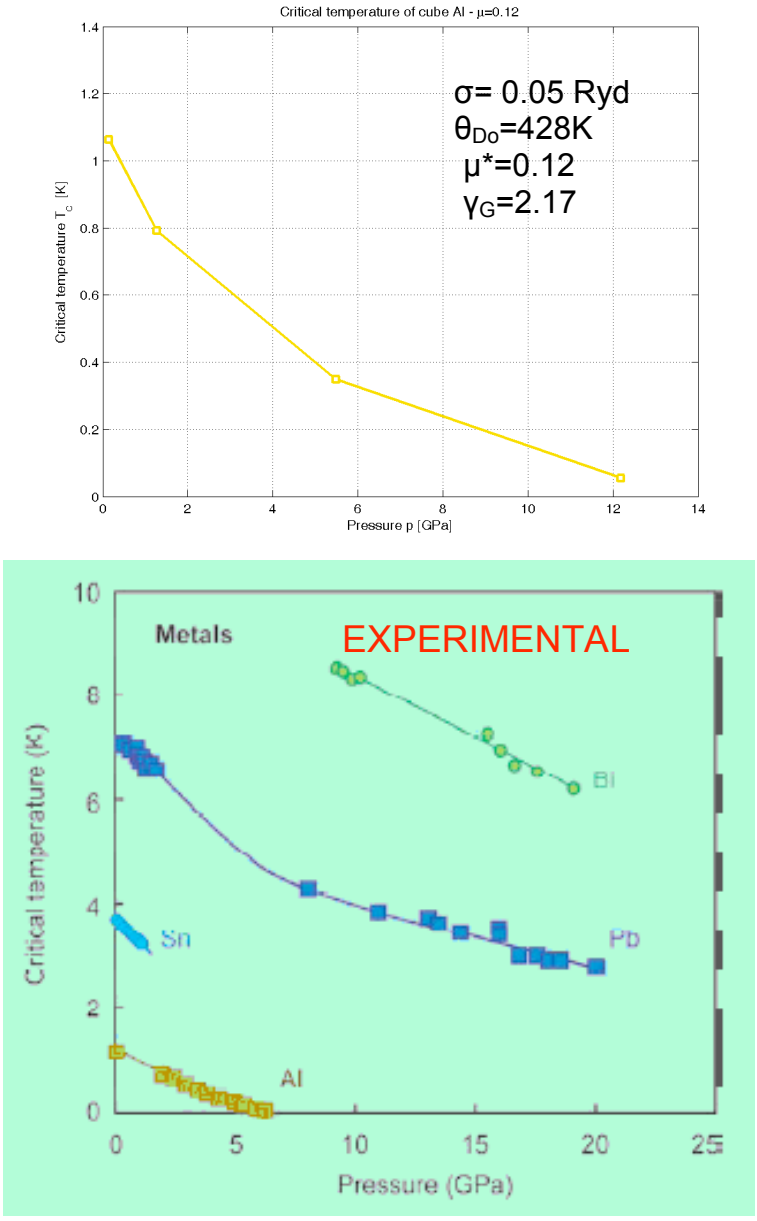

Fig. 34 T_c dependence on pressure in Aluminum. The plot above shows the theoretical calculated values while the plot below shows the experimental data (from C. Buzea and K.Robbie, Supercond. Sci. Technol. 2005).

DFT calculation of T_c can be also extended to cases of simple deformations that cannot be easily reproduced experimentally. For instance, we can study the dependence of T_c on single strain mode deformations to determine the ones that degrade the superconducting properties the most. To carry out experimentally such study would be extremely difficult because of the superposition of many elemental deformations modes present in even the simpler superconducting wires. Fig 3.5 shows the calculated dependence of T_c on uniaxial strain (both compressive and tensile) for Aluminum.

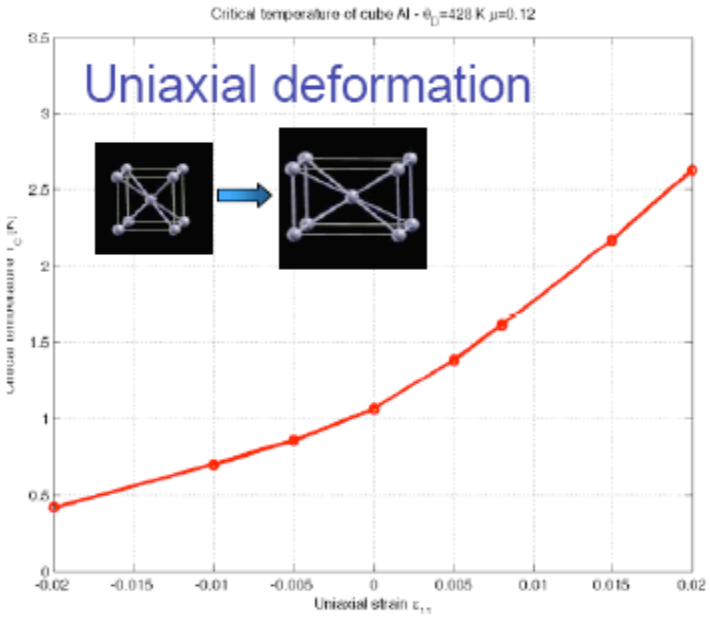

Fig. 3.5 T_c dependence on uniaxial strain in Aluminum.

We are currently performing multiple calculations to determine the T_c dependence on multiple elemental strain modes in Aluminum and Niobium. The Wannier function formalism opens the possibility to extend the study of the T_c-dependence on strain to unit cells characterized by an higher number of atoms and, therefore, efficiently treat the T_c dependence on strain for the case of a Nb_3Sn crystal and, possibly, of a non-stoichiometric Nb_3Sn super-cell. A full *ab-initio* description of the Nb_3Sn T_c dependence on strain states will be a valuable building block for the most recent scaling equations based on microscopic models. Furthermore, the computational study of non-hydrostatic deformations in Nb_3Sn crystals has the potential to elucidate some of the mechanisms behind the strong J_c strain-dependence observed in Nb_3Sn wires under the expected bending and transverse loading modes. DFT shows promise for fundamental predictions of strain effects on LTS superconductors in the near future.

During the coming year we plan to focus on the modeling of the lattice distortion of Aluminum, Niobium, Nb_3Sn and Nb_3Al. Our first goal is to quantitatively understand the reasons lying behind the different sensitivity of these superconducting materials on hydrostatic and deviatoric strain components. Secondly, and again on a quantitative basis, we aim to understand the reasons behind the different magnitude in strain sensitivity showed by Nb_3Sn and Nb_3Al. The quantitative understanding of these behaviors would be a good starting point for the design of improved materials and a good indication for possible novel wire architectures aimed at minimizing the most adverse strain tensor states.

4 SUBTASK-3: EXPERIMENTAL STUDY OF TRANSVERSE STRESS EFFECTS ON SUPERCONDUCTING CABLES

4.1 Introduction

Following the interesting results obtained with the single turn experimental setup, described in detail in last years report, it was decided to retain all the information learned with that experimental rig and build a new experimental setup that could perform the same type of measurements but that improved the ease of sample fabrication and mounting (the most challenging part of the single turn experimental setup). At the same time, a facility was updated and became available at the NHMFL which uses a superconducting split magnet, giving us the opportunity to use a hairpin design for the test sample. The hairpin design gives more flexibility over the fabrication process. Additionally, with minor changes to the sample holder, it was possible to test different size cables including, single strand, triplet and 45-strand cable. In this section we present a detailed description of the hairpin experimental setup as well as a summary of the experimental results.

The goal of this experiment is to measure the effect of transverse load on the critical current of a superconducting cable. The load is applied mechanically by pulling multiple wedge pieces that transversely displace pieces that, ultimately, applies the load on the cable located inside its holder. The components of the probe used for the experiments will be described in details and the measurement techniques will be presented. The system of linear actuator outside the cryostat was used to apply the load and this is the same system used in the previous version of this experiment. A load cell was mounted outside the dewar to measure the vertical load applied to move the wedge upward. This force is then easily related to the actual transverse force applied to the cable by geometrical means as described in section 4.5. The experimental results are presented and discussed.

4.2 System requirements and probe description

The primary test facility used here is located at the NHMFL in Tallahassee, FL. The magnet system used to apply the external field is comprised of an Oxford superconducting split magnet with a 30x70 mm slot where the sample can be mounted and which provides the magnetic field of 12 T uniform over a 150 mm length. Holmium pole pieces can be inserted in the center of the coils to reach 14 T magnetic field but this configuration was not used in the experiment.

A picture of the magnet system is shown in Fig. 4.1 showing the slot (Fig. 4.1b) through which the sample is lowered. The magnet is located inside a cryostat. Once the sample is inserted into the cryostat and through the bore of the magnet, it has to be held in position so that it does not move while the load is applied with the linear actuator. A remotely actuated sliding pin is used to lock the bottom of the sample holder to the cryostat. Certain flexibility is required in the positioning of the sample inside the magnet. This is obtained by having a slightly oversized hole at the bottom of the probe where the pin slides in. On the top of the cryostat, outside, a bellows is mounted between two plates and the flange of the probe is resting on top of the plate. The bellows is used to adjust the vertical position to within 1".

An overall schematic view of the magnet system is shown in Fig. 4.2 also showing how the probe is positioned inside the magnet. In the same figure the linear actuator is shown. The actuator is operated by a motor.

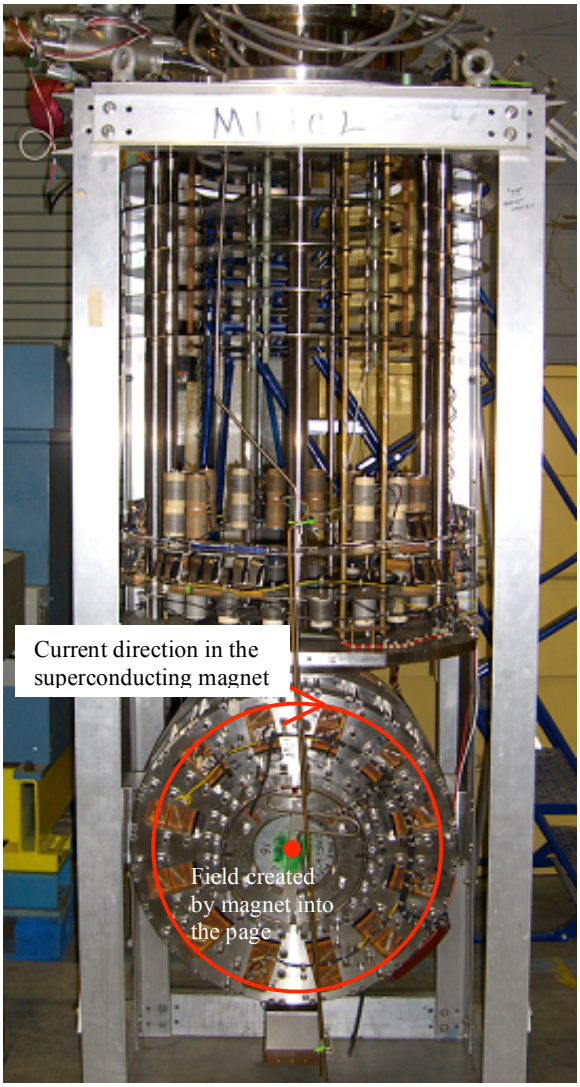

(a)

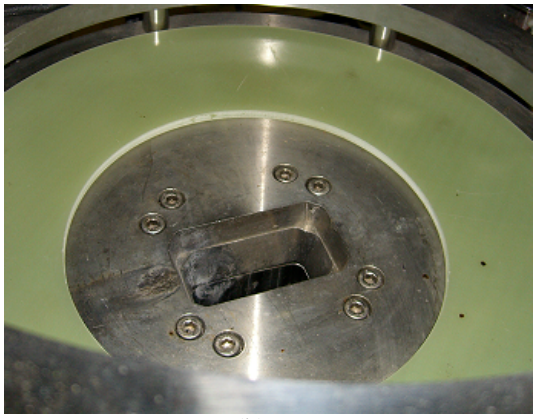

(b)

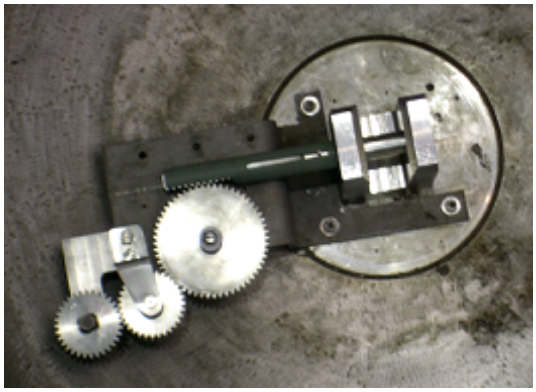

(c)

Fig. 4.1 (a) Split magnet outside the cryostat with coil current and generated magnetic field directions. (b) Slot where the probe will be lowered to be positioned in the center of the magnet. (c) Remotely actuated sliding pin used to lock the probe in position.

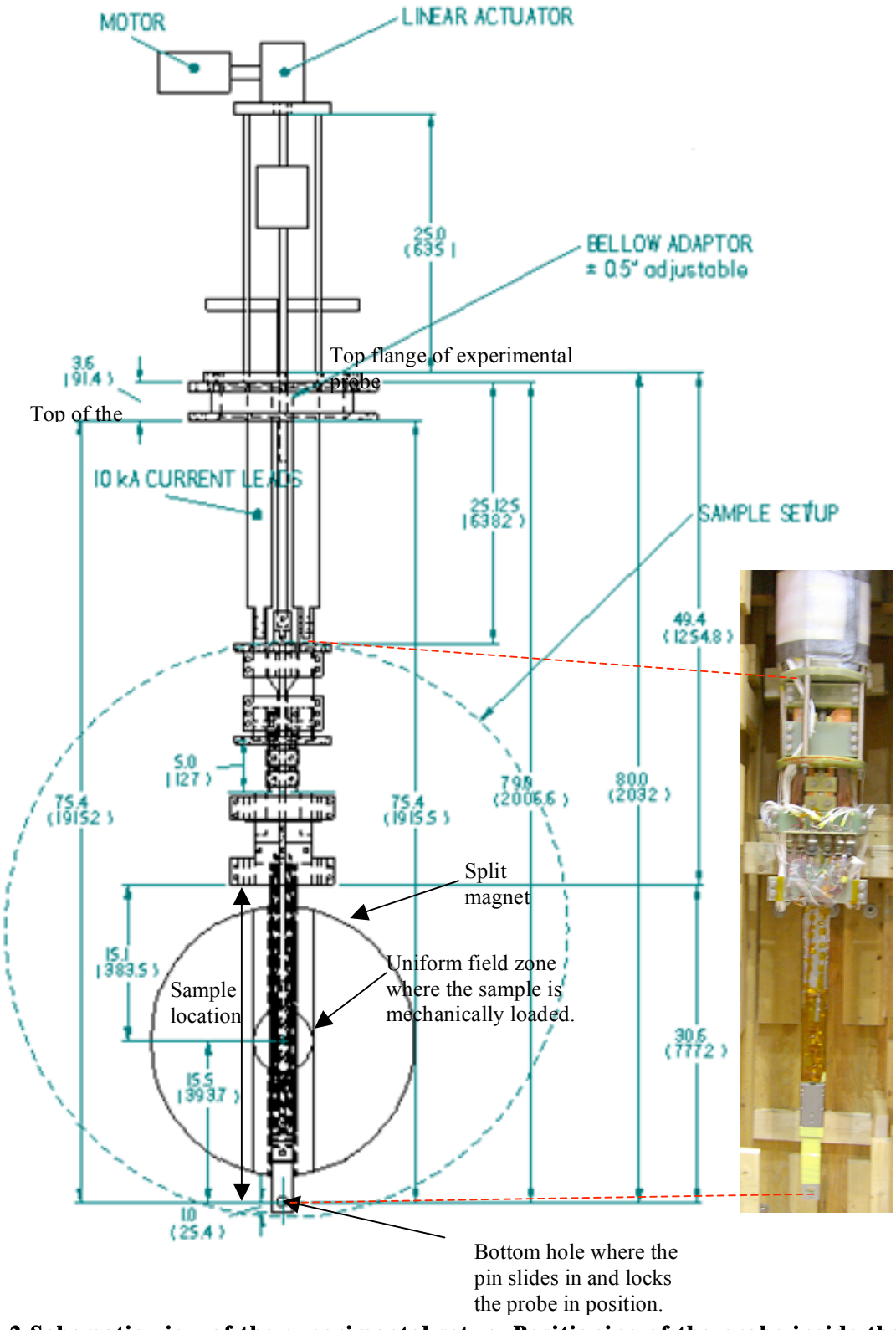

Fig. 4.2 Schematic view of the experimental setup. Positioning of the probe inside the split magnet.

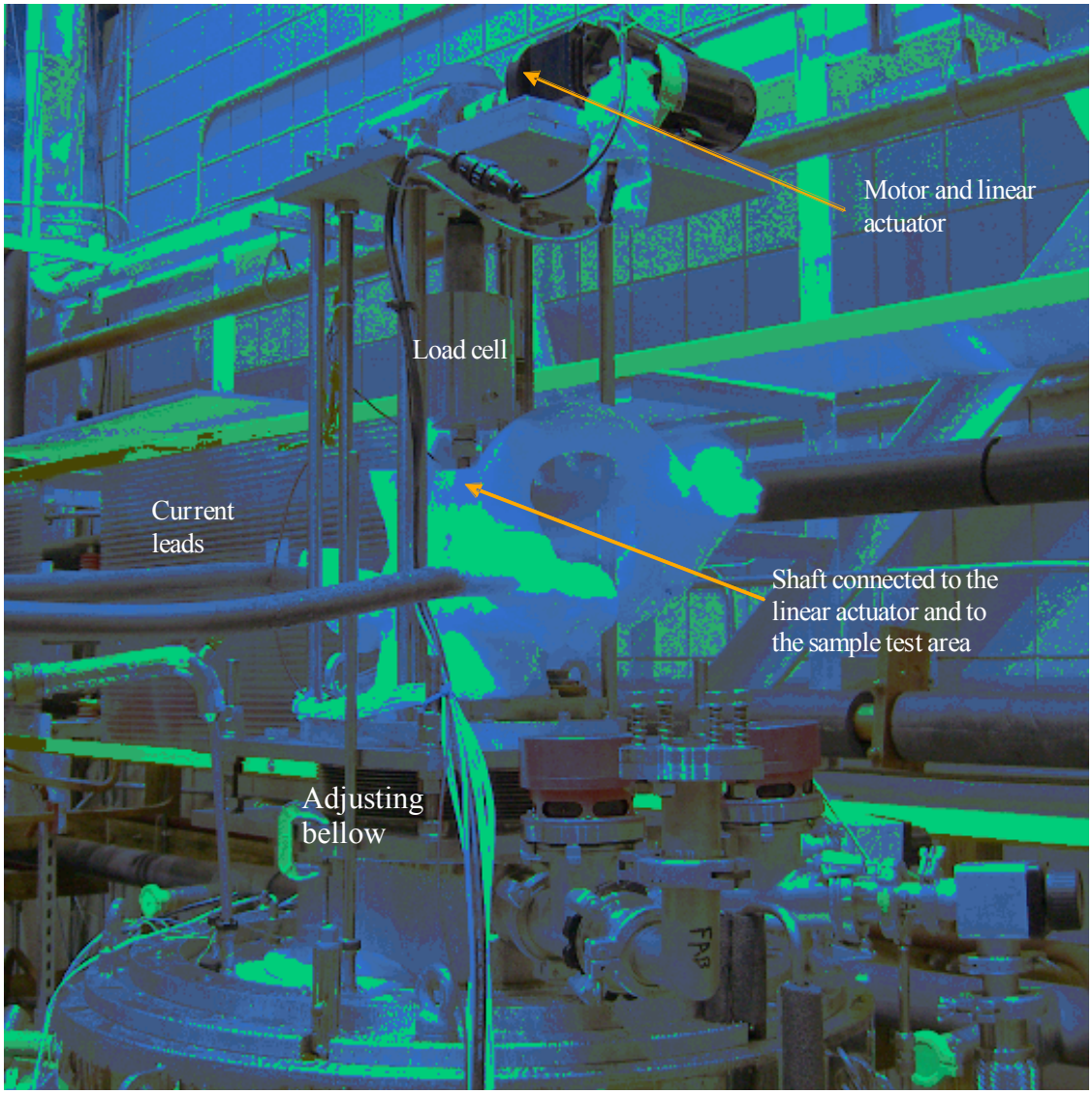

Fig. 4.3 Probe inside the dewar. The picture shows the top flange and the bellows used to adjust the height of the probe so that it can be easily connected to the pin sitting on the bottom of the cryostat. The linear actuator and the motor used to operate it are sitting on a plate. The linear actuator is connected to the cylinder that contains the load cell and connects the actuator to the shaft connected to the wedge at the sample area.

The probe used for this experiment is the same as the one described in last years report. The copper current leads which attached to the 10 kA vapor cooled leads were re-designed to improve the flexibility and to adapt the joint design to the new sample structure (Fig.4.4).

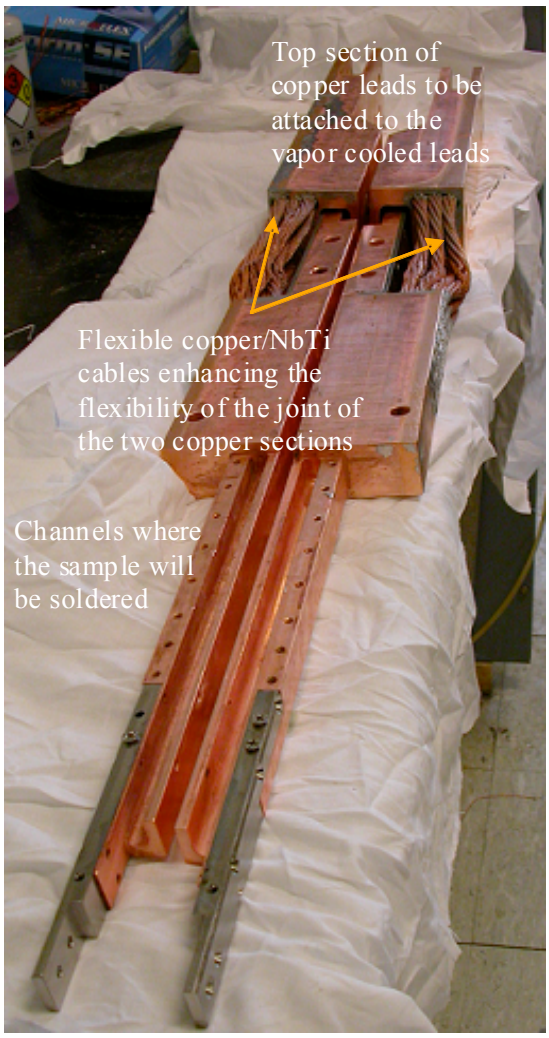

(a)

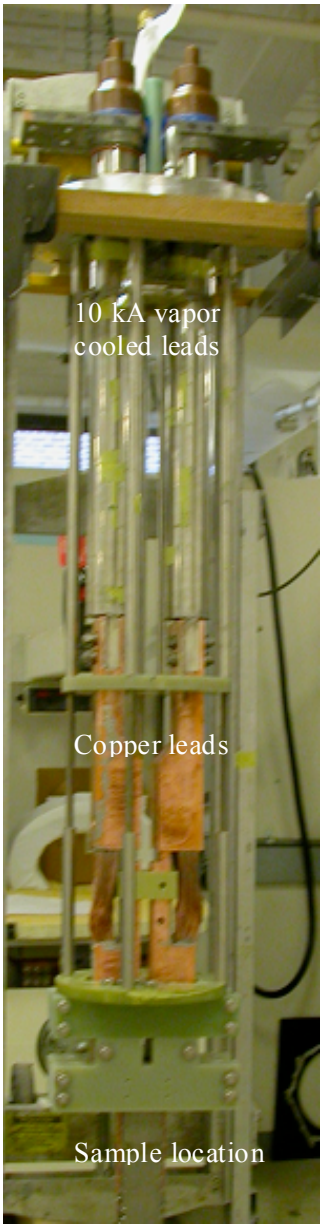

(b)

Fig. 4.4 (a) Copper leads: top section is connected to the vapor cooled leads, the bottom one is where the sample is soldered. (b) Probe set up with 10 kA vapor cooled leads and copper leads.

4.2 Sample area structure

The split magnet system creates a field perpendicular to the vertical direction and gives the flexibility to use a hairpin sample with legs that connect to the current leads without having to bend the sample out of its plane (Fig. 4.5). The field and current direction create a natural load in the same direction as the mechanically applied load.

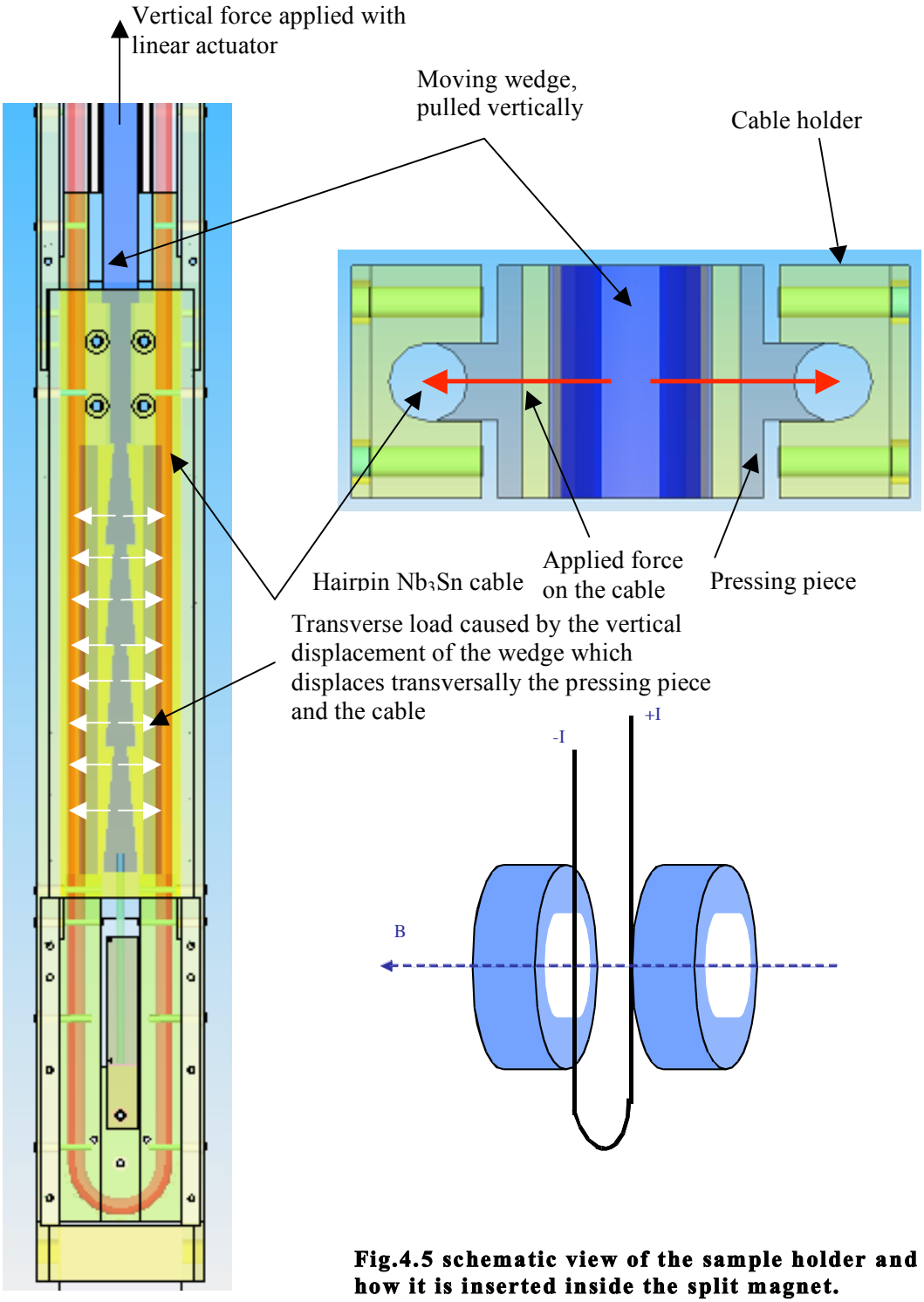

Fig.4.5 schematic view of the sample holder and how it is inserted inside the split magnet.

The load is applied to the sample using the same technique as the previous experimental setup. To ensure uniformity of the load applied over the length of the sample, the piece moving vertically and applying the load transversally is segmented into multiple wedges. Next to this moving piece there are two matching pieces (one on each side) that are constrained vertically and can only slide horizontally. These touch two pressing pieces underneath which the sample is located (the sample is pressed in between the holder and the pressing piece). The matching wedge pieces are made of 316 stainless steel. This is a strong and non-magnetic material. The wedge pieces were cut simultaneously using the EDM method to have very high tolerances. The high tolerance is necessary to prevent any imperfections which could create an undesirable localized force accumulation which.

The main advantage of this design compared to the one described last year is that the sample is straight, making it much easier to fabricate and handle. The heat treatment structure is much smaller that the previous design (circle 115 mm in diameter compared to a block 30x70 mm). Those dimensions allowed the use of a smaller furnace and the heat treatment of multiple samples at the same time. The cooling conditions of this design are also better since the helium venting is flowing parallel to the cable. The entire structure was made of a $TiAl_6V_4$ alloy that has an excellent strain matching with Nb_3Sn, and it is a strong enough material to react the forces of the experiment. Another advantage is that the same structure can be used to test different size cables. The only parts that require dimensions specific to the cable size are the holder and the pressing piece, thus reducing the overall cost for the test of multiple samples. Samples can be changed fairly easily (2 days to remove one sample and mount a new one) reducing the overall time of preparation.

A block was used to maintain the void fraction during heat treatment together with some metal strips that maintained the correct distance between holder and pressing piece. The metal strips and the block were removed after heat treatment and the wedge pieces were mounted in their place.

4.3 Sample fabrication

In this section the sample fabrication is described presenting the main characteristics of the experimental setup.

All the samples were cabled in our laboratory. The total length of each sample is roughly 1.45 m. The two joints are each 28 cm long and they are positioned inside the channels (Fig. 4.4(a)) designed into the copper leads that need to be solder filled once the sample is mounted on the probe and positioned properly.

Four different samples were prepared and heat treated but only three of them were tested (single strand, triplet, 45-strand cable). The hairpin sample lies on a single plane and it is bent in a U-shape. It was verified on a dummy cable that the bend is not causing de-cabling of small cables (up to 9 strands) but it can cause significant de-cabling in a 45-strand cable. It was decided to pre-swage this cable inside a titanium tube and then bend it to the desired shape (Fig. 4.6). The cable outside the tube was wrapped with stainless steel sheet and pre-swaged to the desired dimension. The last die used for the 45-strand cable was 0.267” while for the 9 -strand cable it was 0.117” and swaged manually. The other two samples (single strand and triplet) did not require any pre-swaging. All the samples were inserted in their

holders using glass sleeves to avoid sintering to metal parts during heat treatment. The holder section where the load is applied is painted with graphite coating to avoid sintering and leave the bare cable exposed to the mechanical load. Flat plates and lateral bars are used to hold the cable holder in position (Fig. 4.7-4.8). Most of the support structure during the heat treatment is carefully removed after the heat treatment and replaced with a single piece case where the cable, its holder and pressing pieces are positioned together with the wedge pieces as shown in Fig. 9.

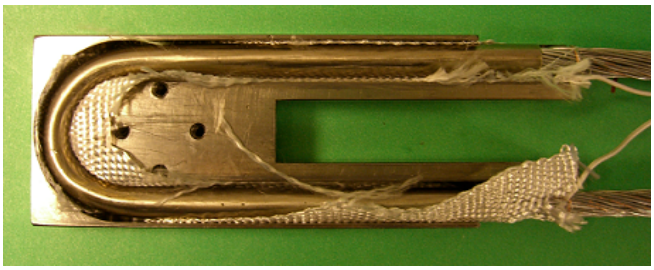

Fig. 4.6 U-shape sample in its holder. Only the 45-strand cable required a supporting titanium tube in the bending area.

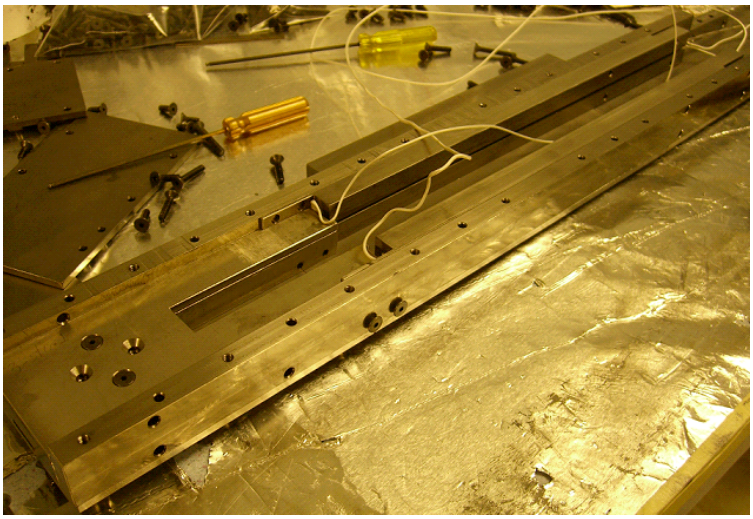

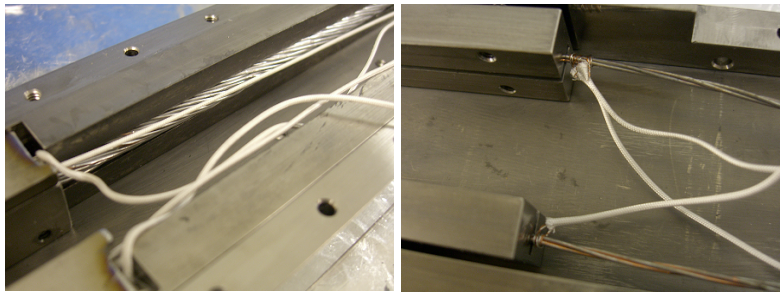

Fig. 4.7 The sample is mounted inside the U-shape holder and the two external holders (top). Bottom wires of the voltage taps (voltage taps 1, 2 and total voltage wire running along the sample to cancel inductive pickup) (bottom left). The top cover of the U-bend is recessed by grinding to be able to bring out the voltage tap wires without damaging

them during the loading process. Voltage taps location at the top of the sample (bottom right).

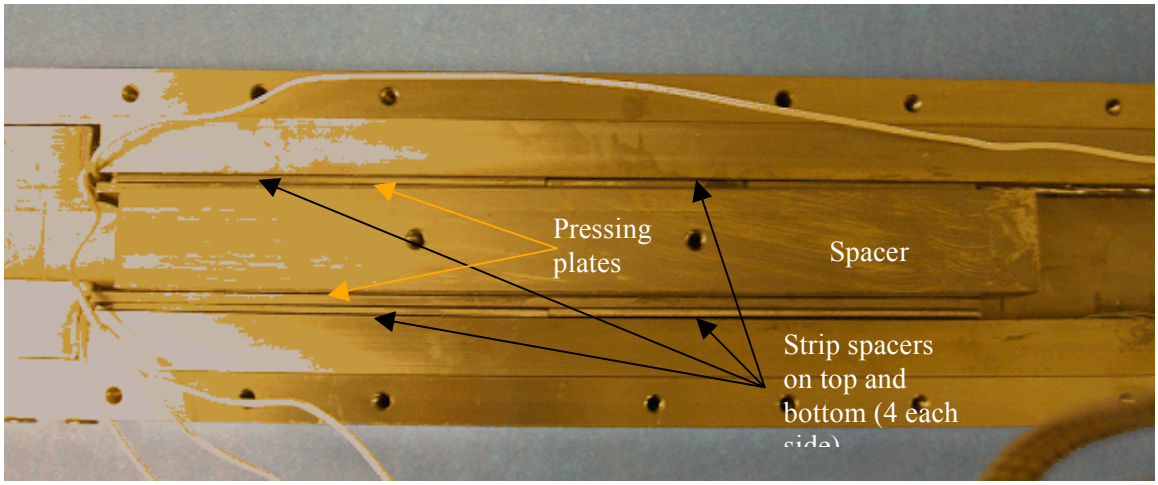

(a)

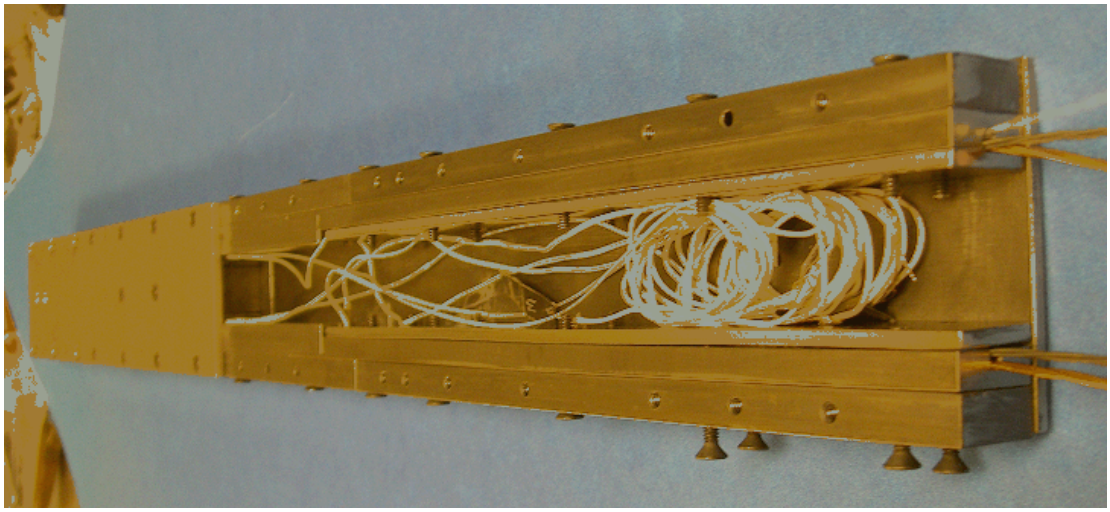

(b)

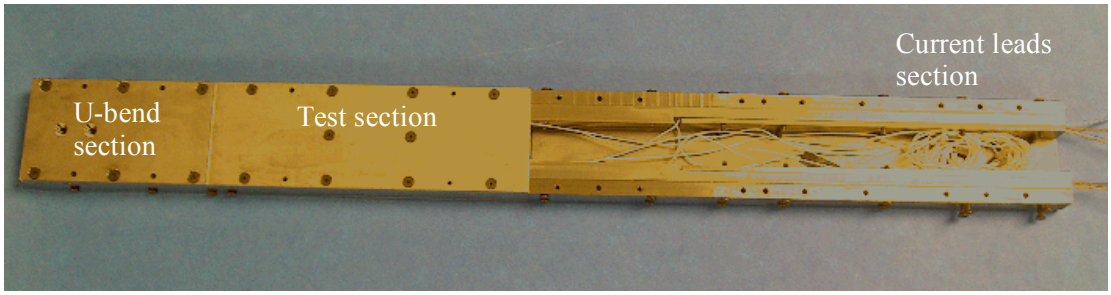

(c)

Fig. 4.8 (a) Bottom voltage tap wires and spacer used to maintain the desired void fraction during heat treatment. (b-c) Sample ready for heat treatment.

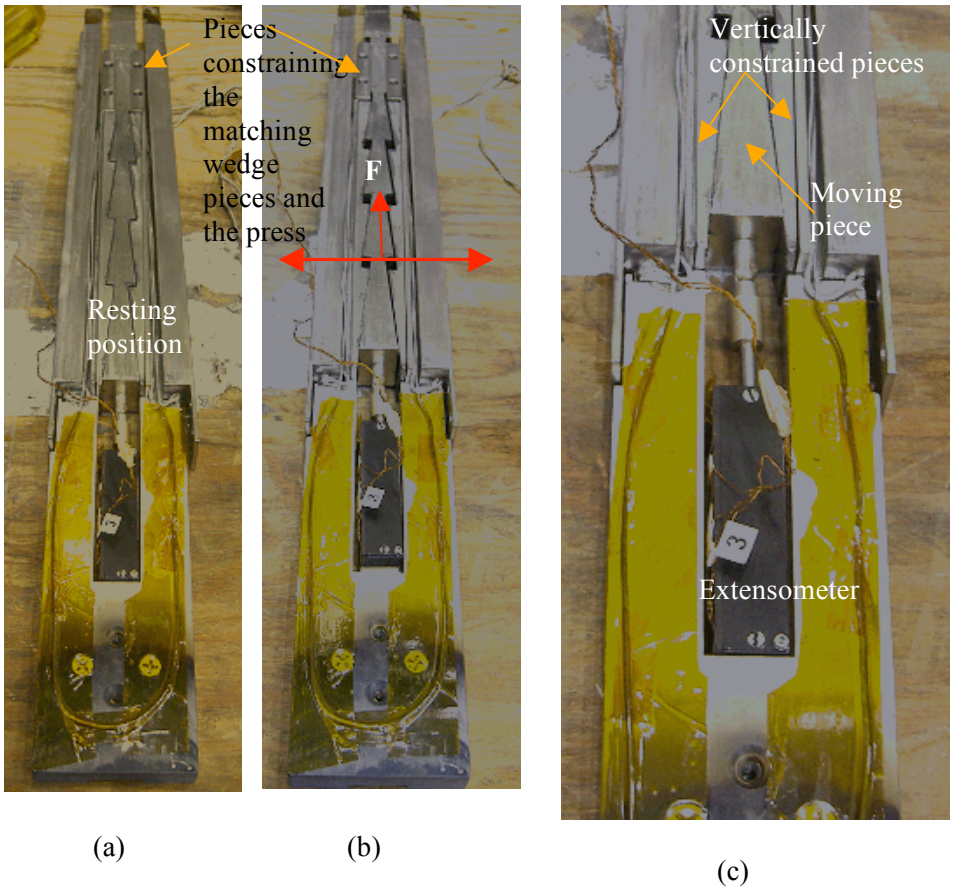

Fig. 4.9 Working principles of the device: (a) resting position of the wedge, (b) vertical displacement of the wedge and movement outward of the matching pieces, (c) displacement measured using the extensometer, (d) heat treatment case and single piece case, (e) sample inside the single piece case ready to be soldered.

4.4 Instrumentation

The experimental setup has been equipped with several instrumentation tools similar to the ones described last year for the previous experimental device. There are three different liquid level sensors to determine the liquid level during the experiment and to maintain the minimum level required for safe operation. Outside the cryostat there is a load cell attached to the linear actuator that applies the vertical displacement to the wedge piece in the cryostat. This unit records the vertical load applied to the experiment. Disregarding friction effects, this load is used to determine the transverse load applied to the sample by geometrical means (Fig. 10, Eq. 4.1). One of the advantages of this configuration is that we used a smaller angle α (5° instead of 10°), but for the same force, we obtain half of the force in the transverse direction (the wedge is pushing two sides at the same time). These two effects balance to give a similar vertical load applied for the two configurations.

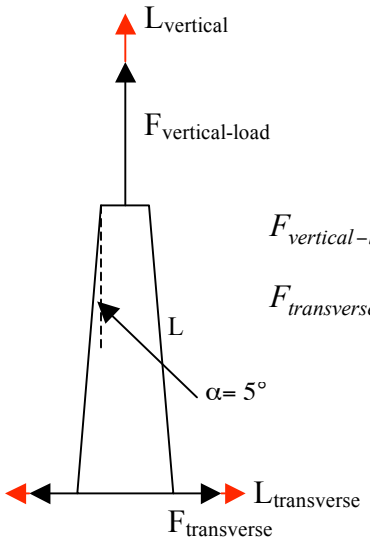

$$F_{vertical-load} \cdot L_{vertical} = 2 \cdot F_{transverse} \cdot L_{transverse}$$

$$F_{transverse} = F_{vertical-load} \cdot \frac{L_{vertical}}{2 \cdot L_{transverse}} = F_{vertical-load} \cdot \frac{1}{2 \cdot tan(\alpha)} \quad (4.1)$$

Fig. 4.10 Schematic view of the forces involved in the experiment and how the transverse force is estimated using geometrical arguments.

Strain gages were mounted on the wide side of the single piece case to verify the uniformity of the load applied since the wedge piece was composed of four sections. Three strain gages were mounted on the front of the case and two in the back (Fig. 4.11). On the same surface a Hall sensor was mounted to verify the direction of the split magnet field and avoid damaging the sample in case the Lorentz load was inward (no support).

An extensometer was mounted on the wedge piece and secured on the sample so that while the load is applied and the wedge displaced, the extensometer remains in position and measures the vertical displacement (Fig. 4.9(a-c)). These measurements were used to evaluate the transverse Young modulus of the tested cables as presented in the following section.

Three pairs of voltage taps were mounted along the sample, two covering each leg and one covering the entire length. The joint resistances were measured at the beginning of the experiment using one wire mounted on the joint and one taken from the voltage tap (Fig. 4.11). The voltage taps are twisted to reduce the inductive voltage as much as possible. The

voltage taps were mounted on the samples before heat treatment and insulated by glass fiber sleeves that can resist the high heat treatment temperatures.

One of the advantages of using a superconducting split magnet to create the background field is the overall reduction of noise level in the system (less than 0.5 μV).

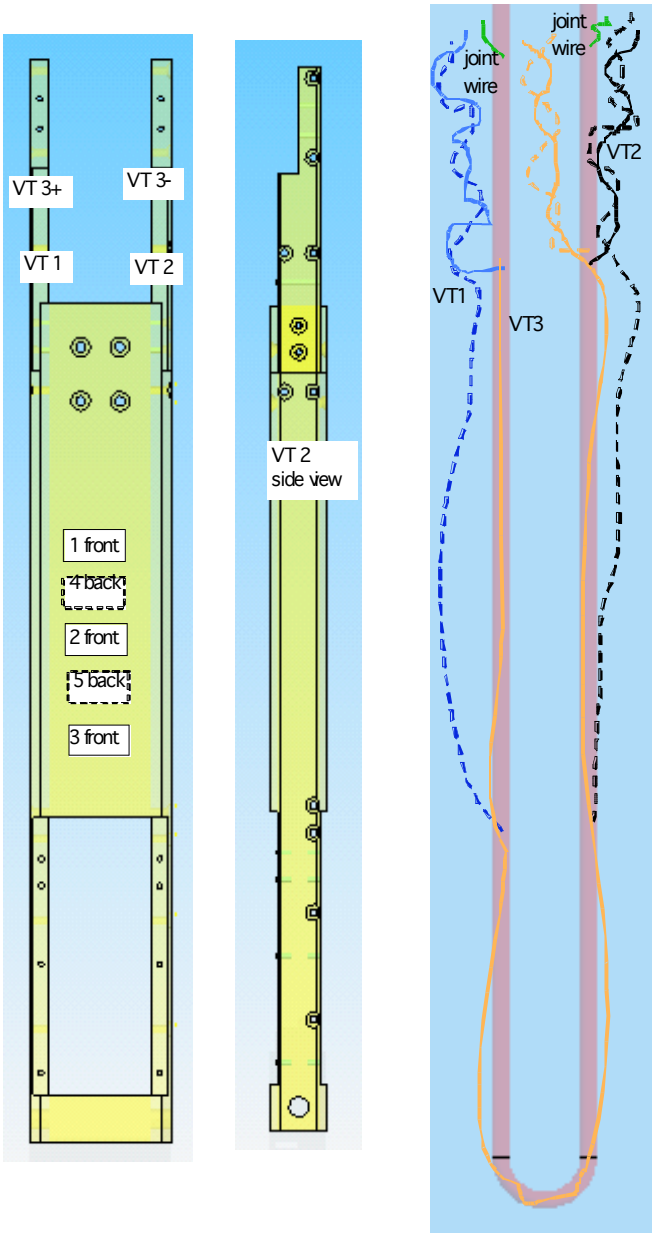

Fig. 4.11 strain gages and voltage taps location on the single piece case and on the sample. VT1 and VT2 cover the two straight legs of the sample and VT3 is the overall sample voltage.

Fig. 4.12 is a comparison between the measured strain gage values and the estimated strain gage values using ANSYS®. It can be seen that the estimated values are roughly twice the average of the measured ones but follow the same trend. The difference could be due to the simplicity of the model that disregards any friction and interaction of the pieces of the experiments and simply considers the case geometry loaded by a transverse force. Additionally, the measurements show similar but not identical values. This could be due to some tilting of the wedge piece or some friction effect (the wedges pieces and their matching part were coated with graphite to reduce friction as much as possible). Strain gages 3 and 4 (SG3-SG4, bottom gage) read the lowest value as expected (the bottom of the wedge is the last to feel the pulling force).

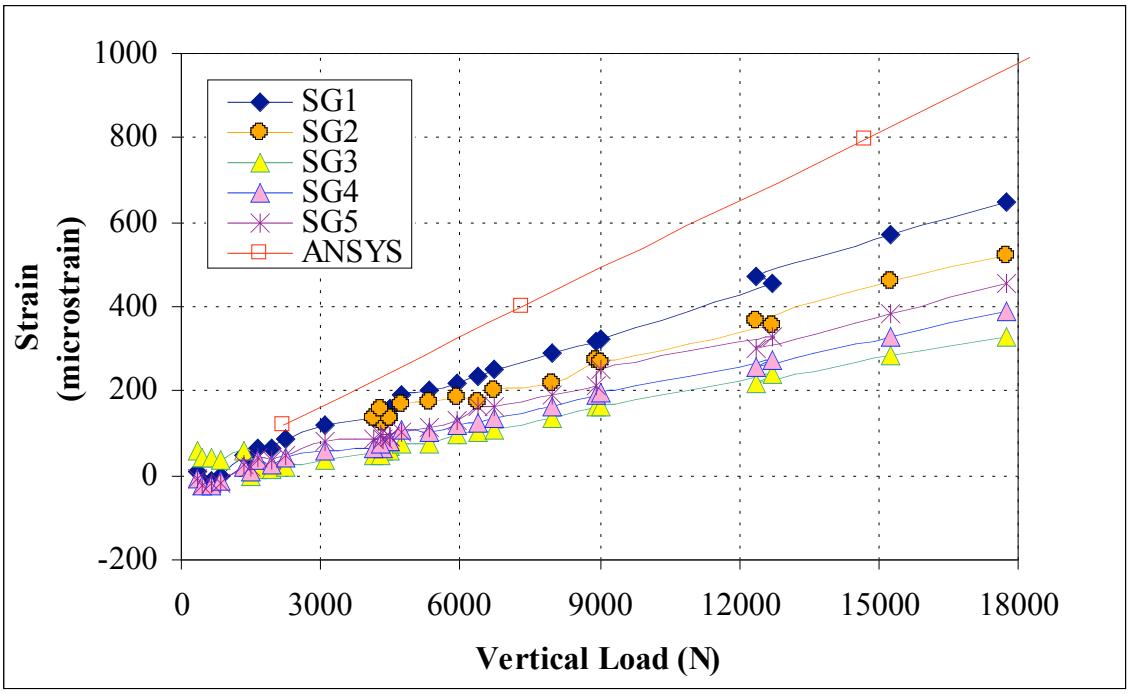

Fig. 4.12 Comparison between measured strain gage values and computed values using the ANSYS code as a function of vertical applied load.

4.5 Experimental results and discussion

A single strand, triplet, 9-strand cable (not tested) and a 45-strand cable were prepared. The different samples use the same type of wire (Internal Tin, Oxford shown in Fig. 4.13) and differ only for the number of strands used. The 45-strand cable is hybrid meaning that the first stage was composed of one copper strand and two superconducting strands (45 strands cable is 30 superconducting and 15 copper strands). The triplet has a twist pitch of 45 mm, the 9-strand cable has a 3x3 cabling pattern (twist pitches of 45 mm, 85 mm) while the 45-strand cable has a 3x3x5 cable pattern (twist pitches 45, 85, 125 mm). All the samples have the same cable pattern 3x3x4 with twist pitches of 45 mm, 85 mm and 125 mm for the three stages respectively. The main properties as given by the manufacturers are given in Table 4.1.

TABLE 4.1 MAIN PROPERTIES OF THE WIRE USED IN THE EXPERIMENTS.

December 2007 samples				
Strand manufacturer	Oxford			
Strand Type	Internal Tin			
Filament Material	Nb_3Sn			
J_c (12 T, 4.2 K)	1014 A/mm^2			
Diameter	0.82 mm			
Copper/non-copper ratio	1.04:1			
Number of strands	1	3	9	45
Average cable diameter (mm)	0.82	1.74	3.01	6.72
Cable pattern	1	triplet	3x3	(1Cu+2SC)x3x5

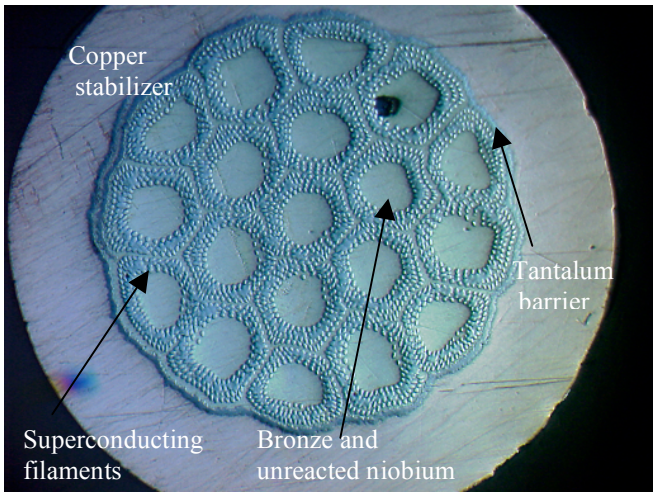

Fig. 4.13 Typical internal tin wire cross section (Oxford wire).

Typically the manufacturer provides the critical current at a certain field (12 T) and the n-value of the strand. The n-value represents the sharpness of the transition (described by Eq. 4.2) from superconducting to resistive state.

$$\left(\frac{E}{E_c}\right) = \left(\frac{E \cdot l_{voltagetap}}{E_c \cdot l_{voltagetap}}\right) = \left(\frac{V}{V_c}\right) = \left(\frac{I}{I_c}\right)^n \qquad (4.2)$$

The critical current is evaluated using the standard critical electric field values of 10 and 100 μV/m. The voltage across the sample is measured as a function of the current and the points where the voltage crosses the critical values (critical electric field*voltage tap length) are the critical current values for that sample. The expected critical current values at different field

are represented in Fig. 4.14. The wire used in this experiment is labeled as Oxford TF. Those values are used to estimate the expected overall current in the different samples (cable current being the product of the single strand current and the number of superconducting strands).

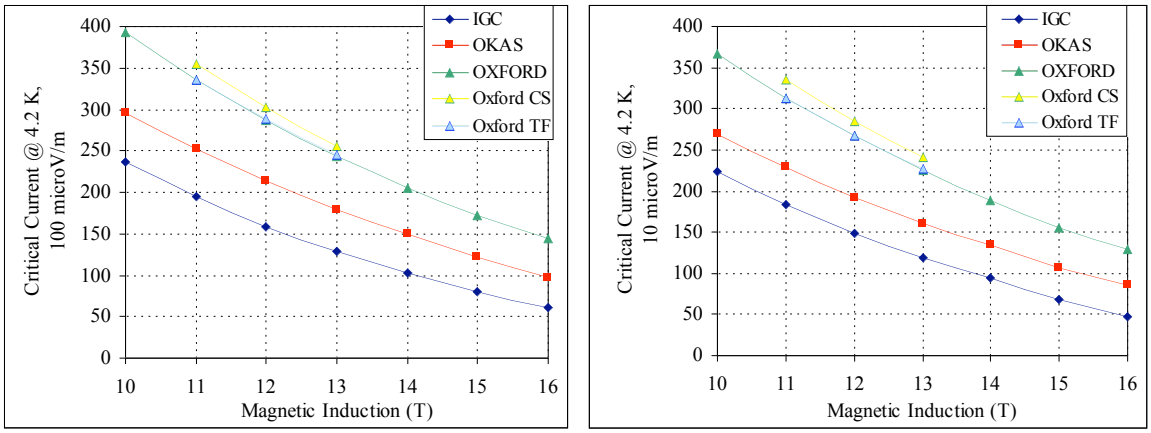

Fig. 4.14 Critical current as a function of magnetic field for single strand samples of the wires used during the experiment. The expected critical value of the cable is simply the product of the number of strands in a cable times the current of one strand.

The campaign of experiments was three weeks long and due to some problems with the locking mechanism at the bottom of the dewar, the 9-strand cable was not tested. The tests took four days between preparation and actual test since every time a sample was changed it needed to be de-soldered from the copper leads and a new sample had to be added and soldered again. As already mentioned, the single piece case and the wedge pieces were the same for all the experiments. The linear actuator was changed between experiments since the single strand test required a finer sensitivity that the other two. The vertical load applied on the single strand was less than 1500 N while for the other two experiments it was 3600 N and 17,700 N, respectively. In addition a very fine vertical displacement had to be applied on the single strand so it was decided to use a micro-actuator (rated capacity 1000 lbs, 0.5" travel). The linear actuator for the triplet and 45-strand cable was the same (rated capacity 10 ton, 2" travel).

The first sample tested was the single strand sample. It must be noted that the experimental setup was optimized for cable and not single strand, so the results for this single strand sample are more sensitive to the measurement techniques and the uncertainty of the mechanical behavior of the system. The testing of the triplet and the 45-strand cables followed the first experiment.

As a general comment, this experimental setup was much easier to handle compared to our previous design, and the compact system obtained by using the hairpin sample allowed a smooth and easy interchange of the samples. A disadvantage of the system is that the background magnetic field cannot be changed as quickly as with a resistive magnet so the measurements at different field were reduced to a minimum.

All the experiments started with critical current measurements as a function of field and the results are reported in Fig. 4.15 with the critical current evaluated at 10 μV/m criteria.

It can be seen that the single strand and triplet reached their expected values while the 45-strand cable showed an initial degradation of 25%. Initially the single strand and triplet showed a higher value than expected with the measurements showing a 40-45 A greater critical current that the nominal value. It is believed that this is caused by the fact a conductive $TiAl_6V_4$ was placed over the current leads for strength purposes. It turns out the plate was lying in a zero field region of the split solenoid. At zero field this material becomes superconductive so that a large fraction of the current might have been flowing inside the plate before reaching the sample itself. The data shown in Fig. 4.15 have been corrected for this effect.

The 45-strand cable shows some degradation but it is far better than any cable tested with the previous experimental setup. The fabrication process has been carried out very carefully but still, unexpected damages might have occurred during the process.

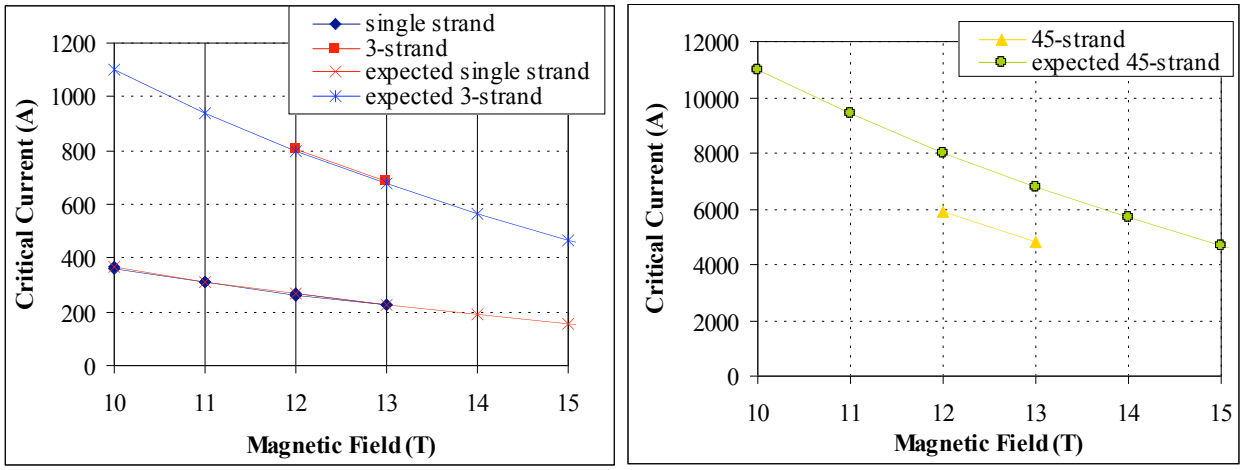

Fig. 4.15 Critical current as a function of field and comparison with the expected values.

Following the critical current measurements the load was applied in small steps at a fixed field of 12 T. The single strand sample has been cycled only once since the time required to test the sample was longer than expected and the micro linear actuator has been reset since it reached its maximum travel. Resetting the linear actuator was a very delicate process in which the load already applied was maintained and the linear actuator removed and reset. After this operation the measurements were concluded with a maximum load applied of 80 MPa and a change of 40% form the initial value. Once the load was removed there was partial recovery of the critical current and a permanent degradation of roughly 20% (Fig. 4.16).

The triplet and 45-strand cable were cycled multiple times as shown in Fig. 4.16. In this figure the critical current normalized to the expected value is plotted as a function of the total load comprised of the applied mechanical load and the natural Lorentz load. The mechanical load is estimated using the measured vertical force from which the transverse force is

calculated (Eq. 4.1). The load is simply the ratio of this force by the cross sectional area of the cable loaded. This area is the product of the length pressed and the diameter of the cable (Eq. 4.2).

$$\sigma = \frac{F_{transverse}}{Area} = F = \frac{F_{vertical-load} \cdot \frac{1}{2 \cdot tan(\alpha)}}{l_{pressed} \cdot D_{cable}} \qquad (4.2)$$

Several observations can be made from Fig. 4.16. First of all, the single strand and triplet do not show any initial degradation. The 45-strand cable shows a ~ 22% initial degradation from the expected values. The single strand starts showing some degradation at loads around 50 MPa while both the triplet and 45-strand cable show degradation at lower loads (35 MPa). Another interesting observation is that the single strand falls off more quickly that the two cables above a 75 MPa load level. This could be due to the fact that the single strand is pressed along its entire length and could be damaged over the entire length while in a cable configuration the load is more localized at the contacts among strands.

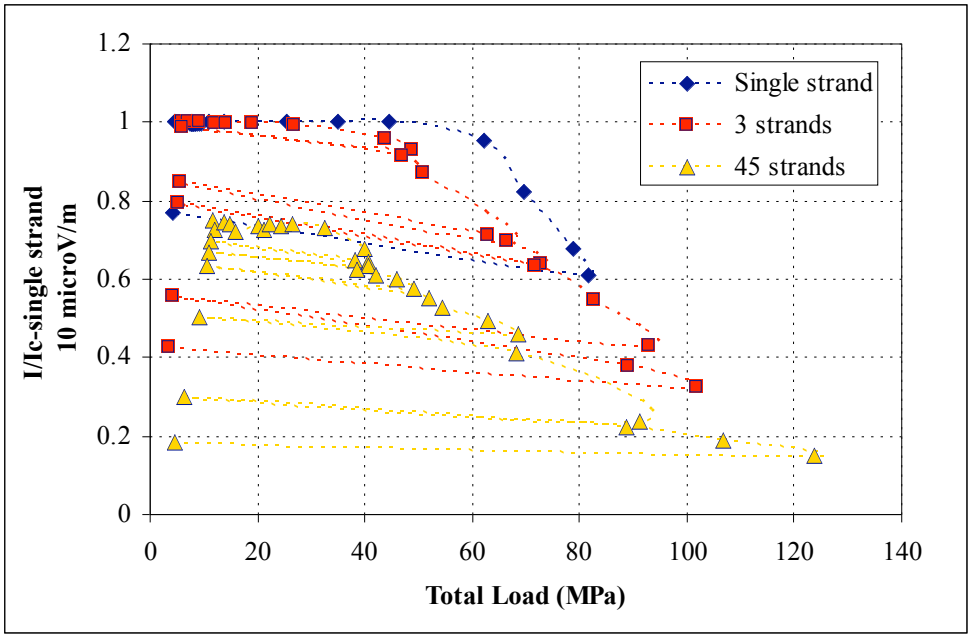

Fig. 4.16 Critical current normalized to the single strand value as a function of total load.

The behavior of the three samples tested is more clearly delineated if the critical current normalized to the **zero-load** value is shown as a function of load (Fig. 4.17). The zero load values coincide with the expected values for the single strand and the triplet while for the 45-strand cable the zero load value is ~ 20% less that the value expected from single strand data. In this figure only the loaded values are plotted (the release values at the end of each cycles

are left out) and again it can be seen that the slope at which the single strand is degrading is more dramatic that the one of the cables.

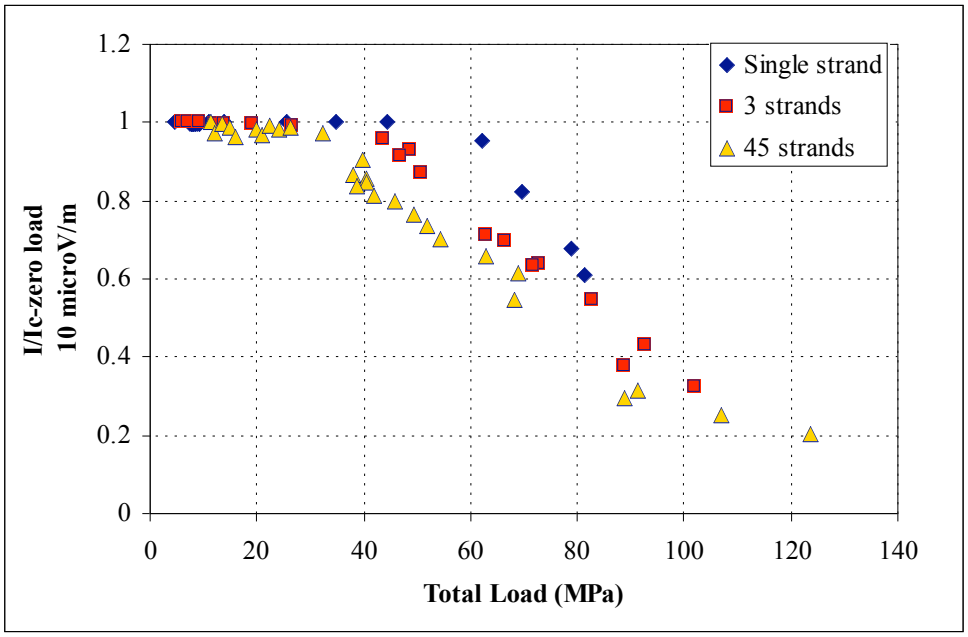

Fig. 4.17 Critical current (normalized to the zero load value) as a function of total load.

4.6 Conclusions

The new hairpin experimental setup was built and successfully tested for the first time with multiple tests on different size cables. The mechanical behavior of CICC cable is a fundamental piece of knowledge required to appropriately design a magnet and be able to obtain the desired performance. Superconducting magnets are the most expensive part of a fusion reactor so a good knowledge of the performance and limitation of these components could reduce the overall construction costs of the machine.

In future work it is necessary to enlarge the number of tests made on subcables in order to be able to understand the fundamental mechanism determining their performance under various mechanical load conditions.

5 SUBTASK-4: DEVELOPMENT OF AN OPTICAL FIBER DIAGNOSTIC FOR MEASUREMENT OF TEMPERATURE AND STRAIN IN SUPERCONDUCTOR WINDINGS

5.1 Introduction

Superconducting magnets can benefit from the use of fiber optic temperature and strain sensors using Brillouin scattering in two ways: quench protection and performance monitoring. Magnet quench protection is the most urgent fiber optic application for large, pulsed cable-in-conduit (CICC) superconductors. A fiber running throughout a superconducting magnet would provide not only a quench protection system, but also a quench locator and a quench propagation diagnostic. Magnet performance monitoring can also be enhanced by providing the first feasible method for real-time measurement of the local temperature and strain distribution in a large superconducting magnet.

5.2 Experimental System

For a discussion on the basics of Brillouin scattering and on previous work that lead to this system, see Reference [17]. Our experimental system consisted of a single frequency Er-doped fiber laser, sending light at 1551 nm through a coupler that splits the light into two different paths, as shown in Fig. 5.1. In the lower path, the light goes through an acousto-optic modulator (AOM), which creates pulses of light of the desired length at the desired rate. The length of this pulse of light in the actual fiber is what determines the spatial resolution of the system. For example, an 80 ns pulse of light corresponds to a spatial resolution of about 8 meters, which is what we chose to use for the strain experiment. After these pulses travel through a circulator to the sensing fiber, which can be hundreds of meters long, the spontaneous Brillouin light is backscattered in the opposite direction.[18]

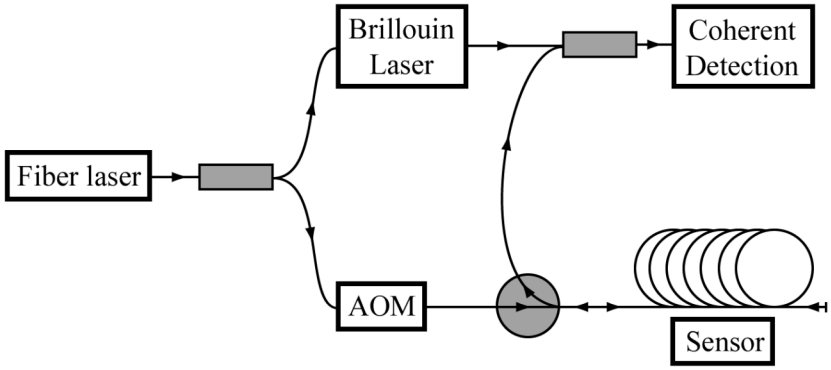

Fig. 5.1: Schematic diagram of the spontaneous Brillouin scattering system.

[17] Magnetics R&D Task D&T-01 FY2008-2012 Proposal.
[18] M. Alahbabi, Y. Cho, T. Newson, "100 km distributed temperature sensor based on coherent detection of spontaneous Brillouin backscatter," Meas. Sci. Technology **15**, 1544-1547 (2004).

The light from the fiber laser going to the upper path is used to pump NP Photonics' Brillouin laser, which is an ultra-narrow linewidth laser (100 Hz).[19] The light leaving the Brillouin laser is combined with the Brillouin backscattered light from the lower path in Fig. 5.1. The Brillouin laser is used as a frequency-shifted local oscillator for the heterodyne detection of the spontaneous Brillouin scattered signal. Since the Brillouin frequency shift is in the 11 GHz range, measuring the frequency of the light within a few MHz is very difficult and expensive. By using a Brillouin laser as a local oscillator, with a frequency nearly 11 GHz lower than that of the fiber laser, the beat signal is heterodyned from the microwave range to the radio frequency range.[20] It is now possible to use a standard detector to measure the frequency shift of the spontaneous Brillouin scattered light.

In order to measure the linewidth of the spontaneous Brillouin scattered light, a MATLAB program was used to take the Fast Fourier Transform (FFT) of the signal. These experiments were done partly under a Department of Energy Small Business Innovative Research (SBIR) Phase I grant whose main purpose was to show feasibility of this measurement approach. In Phase I, there was insufficient funding and time to develop high-speed hardware in addition to the existing system. Instead, the signal was split and run through a General Purpose Interface Bus (GPIB) cable to a second computer, where the signal was recorded. The signal data was run through the MATLAB FFT program to convert the signal data in time to frequency space. Limited by the maximum data transfer speed of the GPIB cable, we were not able to get as many averages of data for the linewidth measurements as we would have liked. A Phase II proposal has been submitted, in which the hardware and support systems for the linewidth measurement will increase the sampling rate by many orders of magnitude.

5.3 Proof of Concept Experiments

Other Brillouin scattering systems have worked as distributed temperature and strain sensors; however, these measurements are near or above room temperature where the relations between the temperature and strain and Brillouin scattering parameters are linear.[21,22] At cryogenic temperatures, these relationships are not only non-linear, but also non-monotonic.[23] To complete the proof of concept, the Brillouin frequency shift, intensity and linewidth were plotted as functions of temperature and strain from cryogenic temperatures up through room temperature.

---

[19] J. Geng, S. Staines, Z. Wang, J. Zong, M. Blake, S. Jiang, "Highly stable low-noise Brillouin fiber laser with ultra-narrow spectral linewidth," IEE Photon Technology Letters **18**, 1813-1815 (2006).

[20] J. Geng, S. Staines, M. Blake, S. Jiang, "Distributed fiber temperature and strain sensor using coherent radio-frequency detection of spontaneous Brillouin scattering," Applied Optics, **46**, No. 23, 5928-5932 (2007).

[21] J. Smith, A. Brown, M. DeMerchant, X. Bao, "Simultaneous distributed strain and temperature measurement," Applied Optics, **38** No. 25, 5372-5377 (1999).

[22] X. Bao, Q. Yu, L. Chen, "Simultaneous strain and temperature measurements with polarization-maintaining fibers and their error analysis by use of a distributed Brillouin loss system," Optics Letters, **29** No. 12, (2004).

[23] L. Thévenaz, A. Fellay, M. Facchini, W. Scandale, M. Nikles, P. Robert, "Brillouin optical fiber sensor for cryogenic thermometry," Proceedings of SPIE, **4694**, (2002).

5.3.1 Temperature Experiment

The main goal of the temperature experiment was to characterize the effect of temperature on the spontaneous Brillouin scattering in optical fibers at cryogenic temperatures. One of the most important factors in the design of this experiment was that the fiber needed to be at a uniform temperature during data acquisition. This was confirmed using several gold-chromega thermocouples and a silicone diode. The fiber was wound loosely in a channel cut into an aluminum disk. Including the aluminum lid, the disk was 1 inch thick and 4 inches in diameter, and the fiber channel had an average diameter of 3.0 inches, as shown in Fig. 5.2.

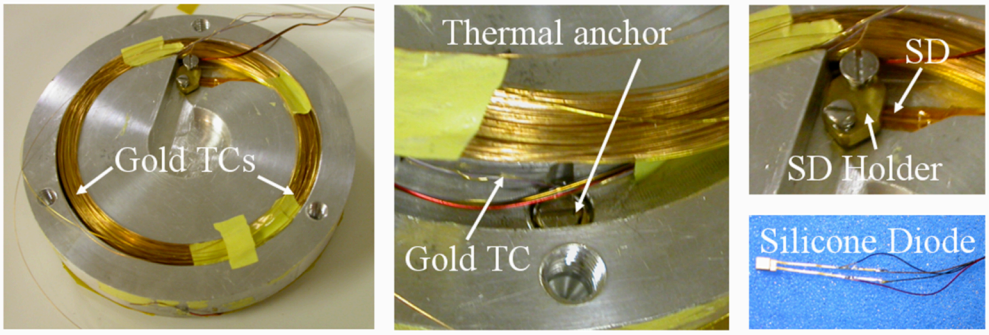

Fig. 5.2: Location of the thermocouples and silicone diode for the temperature experiment.

The frequency shift, linewidth, and power were recorded at many different temperatures from 4 K to room temperature. The frequency shift and linewidth data agree qualitatively with data from other experiments, as shown in Fig. 5.3. A quantitative agreement was not expected for two reasons: 1) our system measured the spontaneous Brillouin scattered light, while Thévenaz's system measured the stimulated Brillouin scattered light, and 2) Thévenaz used standard single mode fiber, whereas we used metal coated single mode fibers with different properties due to the coatings.

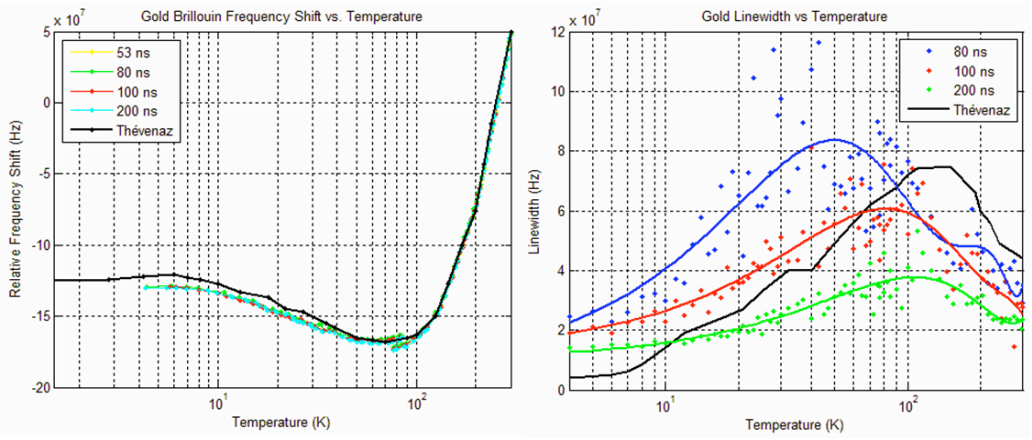

Fig. 5.3: The relative frequency shift and linewidth as a function of temperature from new experiments (color), compared to Thévenaz (black).

As expected, the frequency shift is not a function of pulse length; however, the linewidth is a function of pulse length. The linewidth data is more scattered than the frequency shift data, since it is derived from only 230 averages of the FFT data, compared to the 65,000 averages that were used for the frequency shift data.

On the first day of the experiment, liquid helium was used to generate temperatures from 4 K to 85 K. The probe was removed and warmed up to room temperature overnight, and then liquid nitrogen was used the second day for temperatures from 77 K to room temperature. Fig. 5.3 shows that these two frequency shift data paths are discontinuous, which is due to a change in the fiber properties. The metal coating is applied during the fiber drawing process, which leads to stresses as the fiber cures. The thermal cycle to 4 K and back to room temperature actually cold-worked the fiber, which relieved some of the stresses in the fiber due to the drawing process. This does not eliminate metal coated fibers as potential cryogenic sensors, it simply means that metal coated fibers must be temperature-cycled before they are calibrated as a sensor.

5.3.2 Strain Experiment

Prior to this experiment, there was no data available regarding the effects of strain on the frequency shift, intensity, and linewidth of Brillouin scattered light at cryogenic temperatures. Uniformly straining tens of meters of fiber is not too difficult at room temperature, but when it has to be done in liquid helium most of the commonly used straining systems are no longer feasible. In order to map the effect of strain on the Brillouin scattering parameters as a function of temperature as well, the probe also had to be able to control the temperature of the fiber.

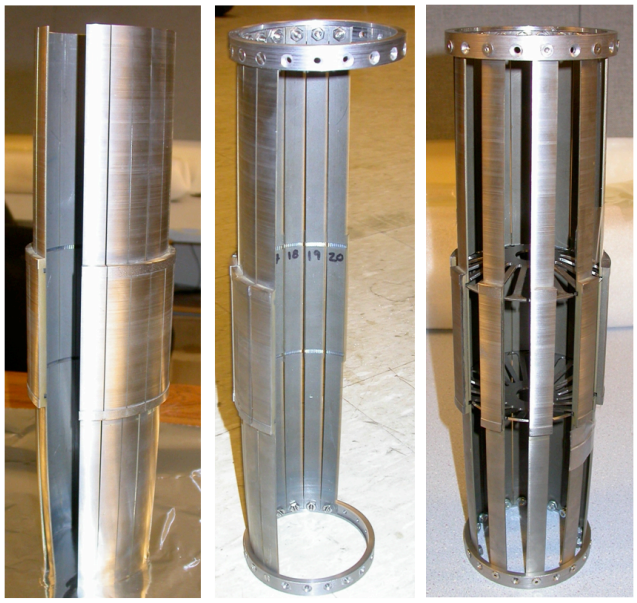

Fig. 5.4: Machined and electric discharge machined (EDM) cylinder (left), view of the cylinder's inside grooves and holders (middle), probe with a few sections removed to see the titanium disks (right).

As in the temperature experiment, it is important that the sample fiber is at a uniform temperature. Liquid helium boiling in a cryogenic experiment will lead to vertical temperature gradients; therefore, the sample fiber should be at as uniform a height as possible. The obvious solution to this problem is to wrap the fibers horizontally around a probe that can expand radially. Since the expected operating strain for ITER magnets is around 2000 με, and fibers can survive about 10,000 με at room temperature, we decided to strain our fibers to around 3500 με. We designed a probe based on the radial expansion of two cone-shaped disks when they are pushed together, as shown in 5.4. The disks were made of a titanium-aluminum-vanadium alloy, Ti-6Al-4V, which has the best cryogenic properties for our experiment.[24] Fingers were cut into the disks which were designed to survive the expected stresses, and also to not buckle under the expected loads. When compressed, these fingers radially expanded a steel cylinder which was sliced into 20 pieces.

Fiber strain gauges were utilized in order to measure the exact strains felt by the sample fiber. Fiber Bragg Gratings (FBGs) are commonly used as strain gauges, but they are not calibrated at cryogenic temperatures. In order to use FBGs as strain gauges at the cryogenic temperatures in our experiments, we first ran a calibration experiment. Three FBGs placed at the bottom, middle, and top of the sample fiber area were used to ensure that each section was expanding uniformly. The location of these FBGs relative to the sample fibers, as well as the locations of the thermocouples and silicone diode can be seen in Fig. 5.5.

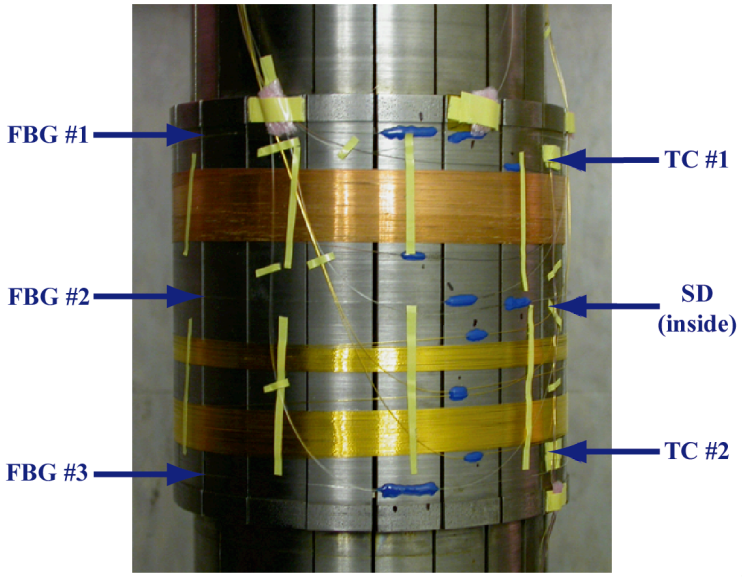

Fig. 5.5: The strain probe after the sample fibers have been epoxied into place. The thermocouples and silicone diode locations are shown on the right, and the FBG strain gauge locations are shown on the left.

A temperature controller was used in conjunction with the silicone diode to heat the fibers to a desired temperature, at which point the fibers were strained to around 3500 με, taking data throughout the strain run. This was done at many different temperatures from 4 K to room temperature to get a good sample of temperature-strain space. By taking these measurements

[24] K. Hanby, Handbook on Materials for Superconducting Machinery, Columbus, Ohio: MCIC, (1977).

over a broad range of temperatures and strains, the experiment allowed mapping of the frequency shift, intensity, and linewidth surfaces as functions of temperature and strain. The following figures include the raw data to visually show how well the surface fit the data.

Throughout the temperature and strain range of our experiment (0-3500 με and 4-300 K), the frequency shift of the spontaneous Brillouin scattered light increased quadratically with increasing strain. A three-dimensional surface was fitted to the data from the strain runs at different temperatures, as shown in Fig. 5.6.

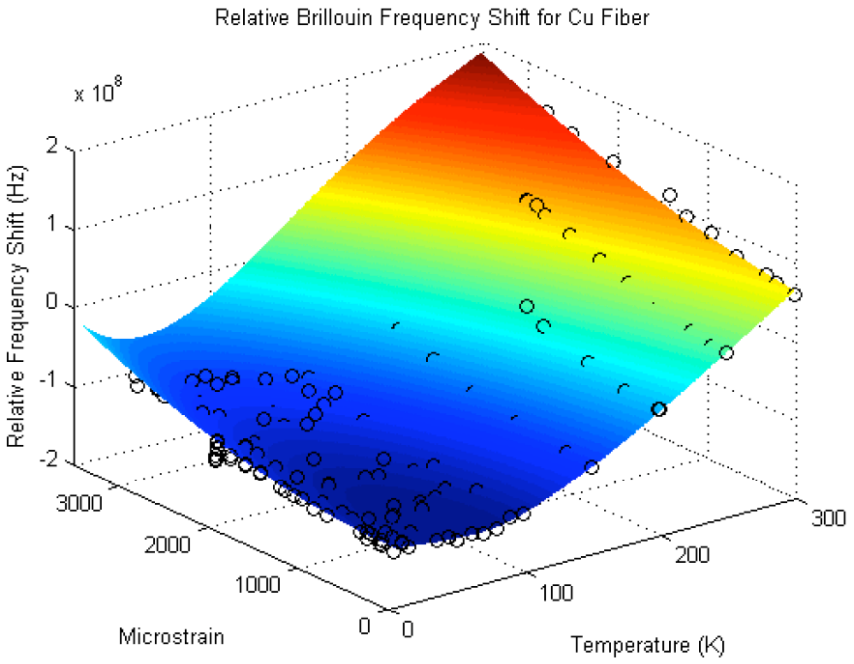

Fig. 5.6: The relative frequency shift as a function of temperature and strain fitted to the experimental data.

The intensity of the Brillouin scattered light was also measured throughout the ranges of temperature and strain. In general, the intensity decreased linearly with increasing strain, as seen in Fig. 5.7.

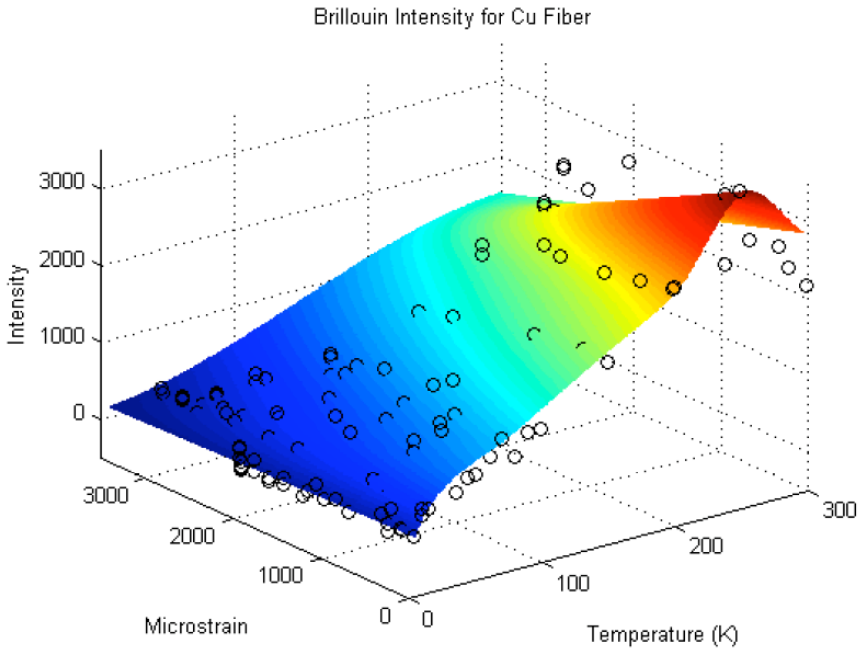

Fig. 5.7: The intensity as a function of temperature and strain fitted to the experimental data.

Analysis of the signal data in frequency space revealed that increasing the strain generally increased the linewidth of the Brillouin scattered light, as seen in Fig. 5.8.

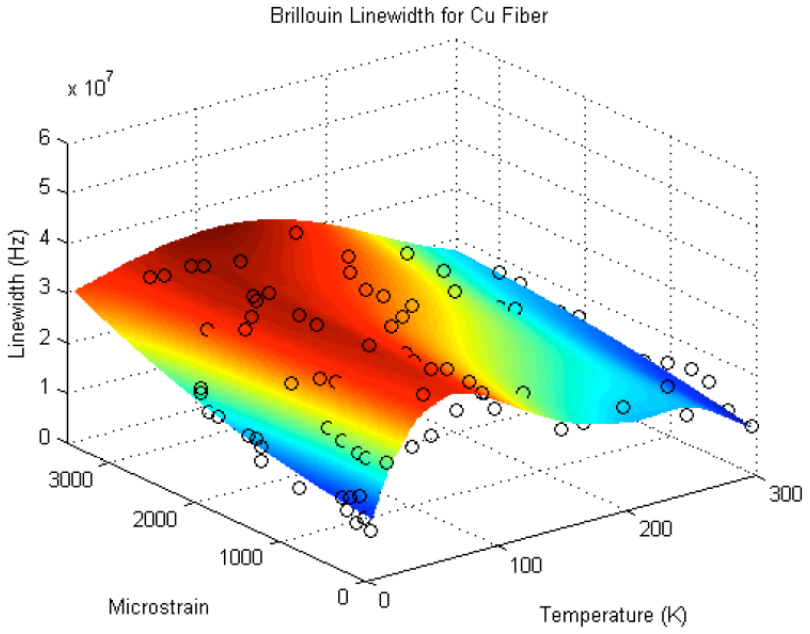

Fig. 5.8: The linewidth as a function of temperature and strain fitted to the experimental data.

Despite the small number of averages, leading to poor statistical data for the linewidth calculations, the general shape of the surface can still be plotted. In order to use our system as an actual diagnostic, these surfaces have to be mapped out much more precisely; however, for a proof of concept experiment, the general shapes of the surfaces are all that is needed.

5.4 Simultaneous Temperature and Strain Calculations

The goal of this system is to be able to measure the spatially resolved temperature and strain throughout the length of the fiber sensor. Using OTDR we can separate measurements and provide spatial resolution. The three-dimensional surfaces shown in Figs. 5.6-5.8 allow us to calculate unique values of temperature and strain, according to the spatially resolved data.

5.5 Using Only Frequency Shift and Intensity

Determining the temperature and strain from only the measured frequency shift and intensity data is possible at room temperature, since both frequency shift and intensity are individually linear with respect to temperature and strain. Since these functions become non-monotonic at cryogenic temperatures, there will be certain regions of temperature and strain that cannot be distinguished. Using Figs. 5.6 and 5.7, we can calculate the temperature and strain based on a simulated measurement. Assuming that the system measures a relative Brillouin frequency shift of -100 MHz and an intensity of 1000, we can look at the set of possible temperatures and strains as shown in Fig. 5.9.

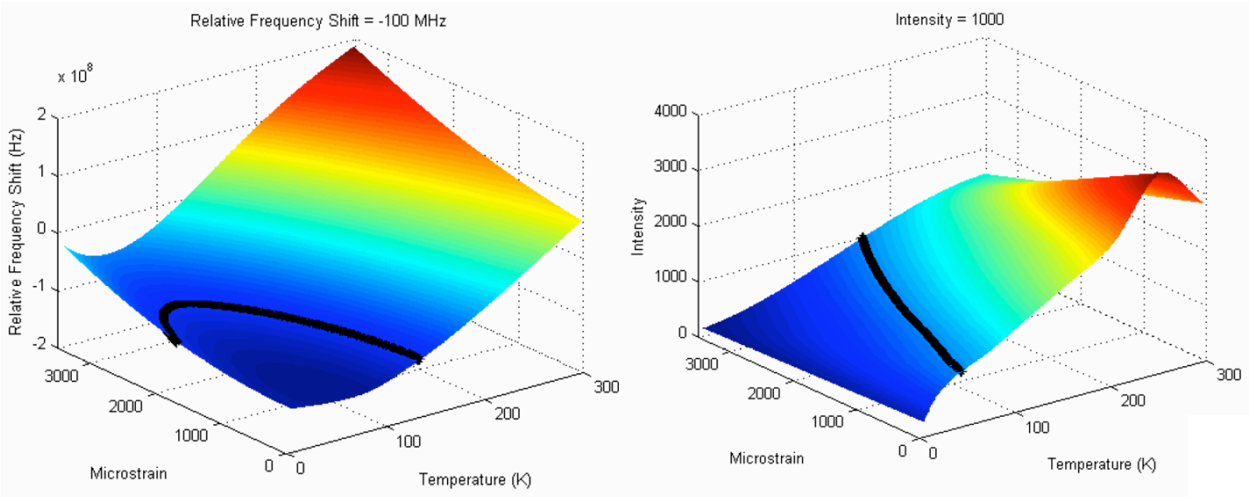

Fig. 5.9: The temperature and strain data sets (black) are found by taking a slice through the surfaces.

The measured temperature and strain are found at the intersection of these two data sets. These data sets, the thicker lines in **Error! Reference source not found.** 5.10, show that the temperature and strain corresponding to the measured frequency shift and intensity are 95 K and 1900 με, respectively.

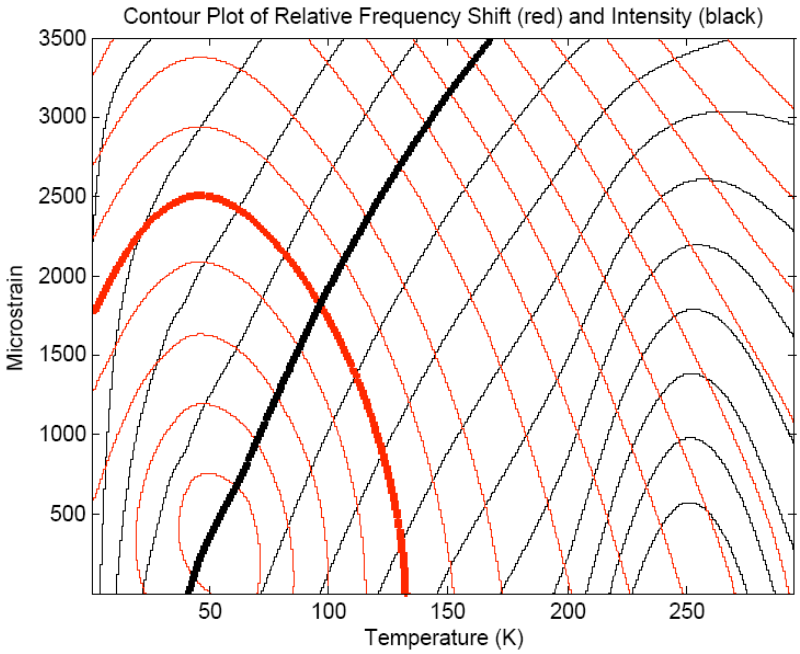

Fig. 5.10: Contour plot of the relative frequency shift and intensity showing that these two measurements alone can usually provide a unique temperature and strain measurement. The thicker lines are the data sets from the example measurements of -100 MHz and an intensity of 1000.

5.6 Using Frequency Shift, Intensity, and Linewidth

There are certain times when the frequency shift and intensity are not enough to uniquely determine the temperature and strain, which is when the third parameter (linewidth) is needed. Using the surfaces generated from the signal data in frequency space, another example measurement can be generated. Assuming that a relative frequency shift of -135 MHz was measured, along with an intensity of 1000, the temperature and strain can not be uniquely determined. The measurement could be 60 K and 700 με, or it could be 45 K and 100 με. Assuming that we also measured a linewidth of 30 MHz, we can determine that the temperature is 45 K and that the strain is then 100 με, as shown in **Error! Reference source not found.** 5.11.

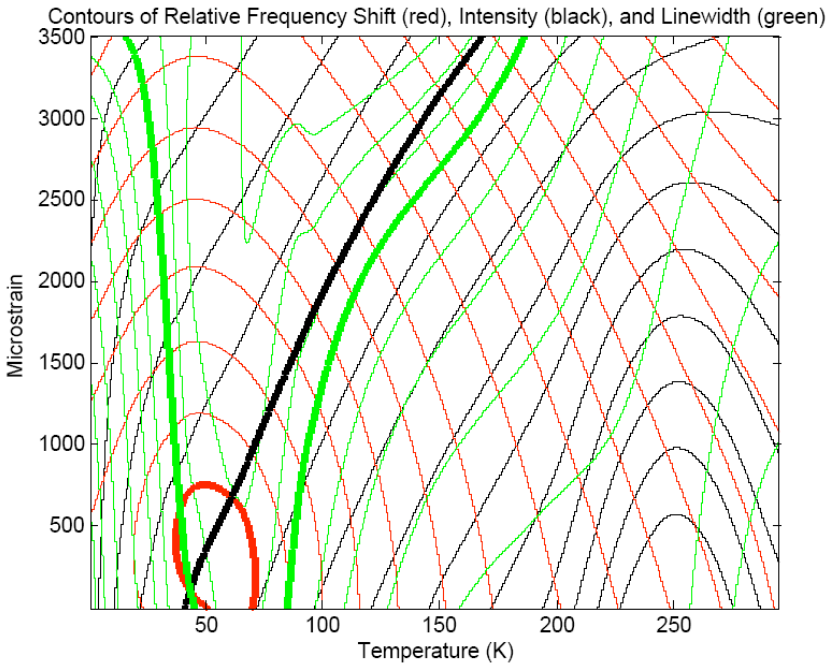

Fig. 5.11: Contour plots of the relative frequency shift, intensity, and linewidth provide a unique temperature and strain. For the example, the frequency shift and intensity provide two potential temperatures and strain, but including the linewidth, the correct temperature and strain is found.

Error! Reference source not found. 5.11 also shows that the temperature and strain can be uniquely determined throughout the temperature and strain space plotted. In the regions where two of the three parameters are parallel, the third is not. Moreover, the third parameter only intersects this parallel zone once, which allows it to distinguish the appropriate temperature and strain.

5.7 Conclusions and Future Work

Using a copper alloy coated fiber, we obtained a spatial resolution of 5 meters at 4 K, and were able to map out the important Brillouin scattering parameters in temperature and strain space. These surfaces proved that a unique temperature and strain can be calculated simply using the frequency shift and intensity for most of the region of interest for superconducting magnets (4-200 K, and 0 – 3500 με). The linewidth measurement can be used as a check, and is sometimes needed to uniquely determine the temperature and strain in regions where the frequency shift and intensity measurements are not enough.

Since the measurement time is on the order of 0.5 seconds, this system can be used as a quench detection system for large superconducting magnets. The spatial resolution allows the systems not only to locate the origin of the quench, but also to track the temperature changes as the quench spreads. During the heat treatment of a magnet, this system can monitor the temperature throughout the magnet to measure the spatial uniformity of the heat treatment, which has previously been done from the outer surface. Depending on the positioning of the fiber in the winding, this system will also be able to provide the first ever spatially resolved strain measurement in an operating magnet.

In order for this system to be used reliably in an actual magnet system, a more precise calibration experiment needs to be run with an upgraded data acquisition system for the FFT data. There are also several engineering issues that need to be solved, including the extraction of the fiber from pressurized, supercritical helium to a room temperature fiber going to the lasers and DAQ systems.

6 SUBTASK-5: DEVELOPMENT OF HIGH TEMPERATURE SUPERCONDUCTING MAGNETS FOR FUSION

6.1 Magnet Code Development

MIT has a leadership role in the development of specialized codes for design and analysis of superconducting magnet systems for fusion and non-fusion missions. These include SOLXPT3D (solenoid systems with 3D transport)[25], QUENCHER[26] (1 ½ D quench simulation), TOKSCTFPF (TF-PF interactions), and MASADA[27] (arbitrary magnetic system sizing and analysis). The most important and state-of-the-art of these codes is SOLXPT3D, which simulates an entire system of coupled solenoids during both baseline operation and quench, such as a tokamak plasma and its interactions with the CS and PF coil systems. The electrodynamic part of this code includes transient field calculations, including eddy currents in passive structures, induced coil currents, and moving circuits, such as the plasma in a disruption. The thermohydraulic part includes helium flow, local heat transfer from the superconducting cable to the helium channel, conduit, and insulation, thermal and helium mixing in a dual-flow channel, and thermal diffusion between layers and pancakes. The loss simulations that are specific to superconductors include hysteresis, coupling, and eddy losses.

SOLXPT3D was used for the design of the magnet systems in TPX and KSTAR. An IO central team code was used for the design of ITER, but SOLXPT3D has been used to check the baseline design and has uncovered operational regimes in which margins had to be improved. At present, SOLXPT3D is more advanced than any other code in the world, because of its ability to make self-consistent and physical transitions between routine operation and quench. It also has superior ability to switch self-consistently between operational modes (e.g. current source-superconducting, current superconducting-no thermal instability, no quench dump, quench detection-resistive dump, voltage source-resistive dump). It is also the only code that can accumulate the conditions in all coils to supply a complete inventory of power supply and cryogenic refrigeration requirements.

The main improvements in SOLXPT3D in the first quarter of 2008, as part of the ITER program, were the addition of realistic simulations of the baseline quench detection method[28]

---

[25] J. Feng, "A Quasi-2D Model for Helium Flow in 2-Channel CICC," Adv. Cry. Eng., V. 49A, 2004, pp. 807-814

[26] A. Shajii, Theory and Modelling of quench in cable-in-conduit superconducting magnets, MIT Doctoral Thesis, April 1994

[27] J.H. Schultz and P.W. Wang, "MASADA: A New Magnet System Analysis and Design Code Applied to Conceptual Design," IEEE Trans Applied Superconductivity Conf, Pittsburgh, PA, 1996

[28] MAGNETBASE-MIT-FENG-122007-01, Jun Feng, "Summary: a new thermohydraulic-quench code "SOLXPT3D-Q2," Dec 20, 2007

and the development and extensive calibration of the world's first self-consistent code, simulating routine operation, leading to quench[29]. The combined operations-quench code is now called SOLXPT3D-Q2. The significance of this development is that, previously, superconducting operation codes and quench codes have been completely separate. Conditions that would lead to quench in an operation code led to numerical instabilities, so that the early development of a quench could not be studied. All quench codes had to use artificial energy additions or temperature rises with an assumption that quench simply propagates in both directions. Experiments have shown that this assumption is frequently, but not always true. What's worse, it is most likely to be untrue when the superconductor is the most advanced, since advanced and higher temperature superconductors are more likely to 'percolate' in a partially resistive current-sharing mode, without exciting a thermal instability. SOLXPT3D-Q2 can now examine this mode of behavior and has already observed it, numerically, without having to approximate it as an initial condition. It is probably for this reason that the calibrations against experiment, referenced above, have achieved a closer fit than previous quench codes. The models for ITER disruption-quench events with moving and 'shape-shifting' plasmas are shown in Fig. 6.1.

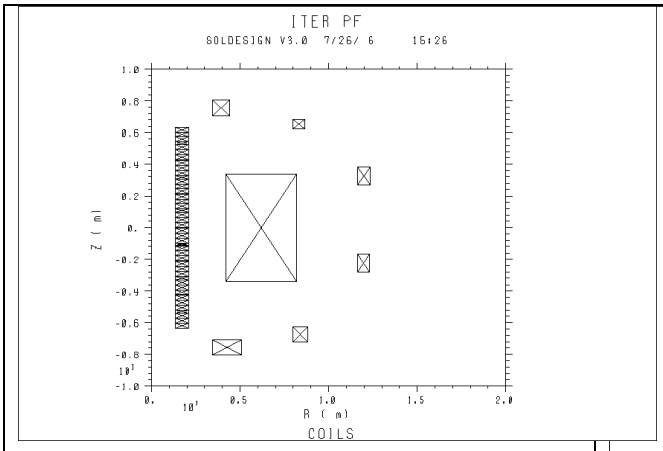

Fig. 6.1a) Baseline scenario, Air-core

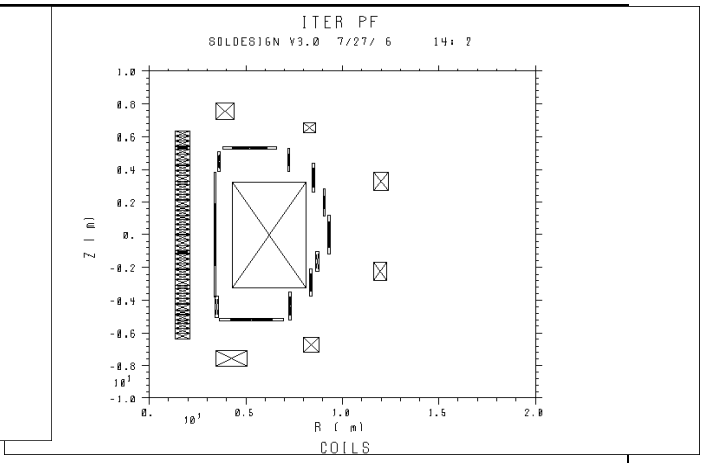

Fig. 6.1b) Stationary plasma scenario, passive structure

[29] MAGNETBASE-MIT-FENG-100907-01, Jun Feng and Joel Schultz, "Calibration of SOLXPT3D-Q2 against QUENCHER and SARUMAN," October 9, 2007; MAGNETBASE-MIT-FENG-110707-01, Jun Feng, "Calibration of SOLXPT3D-Q2 vs. Ando quench experiment," November 7, 2007; ITER-USMIT-FENG-011008-01, Jun Feng and Joel Schultz, "Duplication of Takahashi's CS coil quench simulation," January 10, 2008

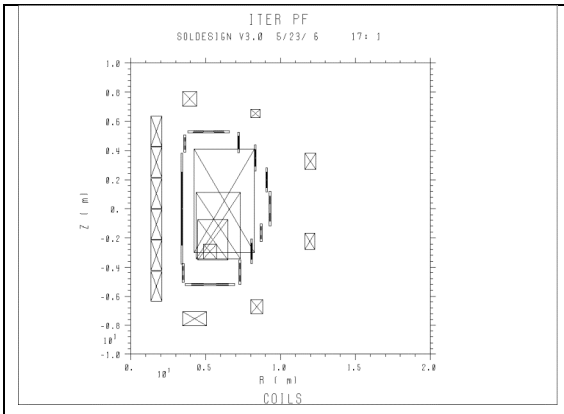

Fig. 6.1c) Disruption, moving plasma, vacuum vessel

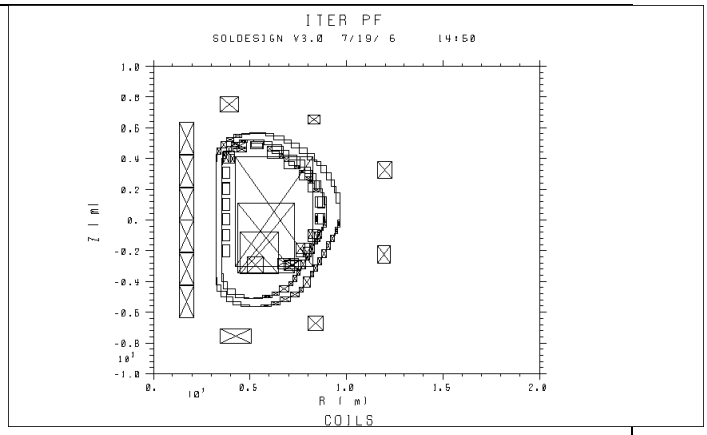

Fig. 6.1d) ITER Baseline Vertical Disruption Event, moving plasma, detailed passive & saddle elements

ITER is no longer supporting SOLXPT3D, despite the fact that it now predicts that some operating modes, such as a vertical disruption at the End of Burn, exceed hot spot temperature allowables, as described below. As develop of SOLXPT3D reverts to the Base Program, the code will occasionally continue to use the ITER CS system as a worked example, but will concentrate on the code development itself. Design cases will shift to DEMO and ARIES, while calibration cases will also draw no state-of-the-art magnet systems, outside of the fusion program.

6.2 Program Goals

The longer term goals of this task are to extend superconducting magnet simulations to include all of the design cases and operating modes that are required by fusion magnets. These include:

1) Simulation of High-Temperature Superconductor (HTS) magnets. The two main requirements are to include subroutines with critical property correlations for HTS materials and to be able to switch models easily between the CICC conductors used for large NbTi and Nb3Sn LTS magnets and the indirectly-cooled tape conductors used for HTS. This requires a topological ‘dry’-mode switch that eliminates the thermohydraulic channel and replaces it with an external conductor cooling model, while allowing direct thermal diffusion between conductors in a winding pack.

2) Improved circuit models: The addition of four circuit “modes”: i.e. current source, voltage source, resistor, and voltage source + resistor in FY08 allows simulation of most of the operational modes in ITER. However, in general, fusion magnet power supplies can be more complex than any of these and have included interleaves, differential power supplies, and coil systems that are partially seriesed and partly independent. A simple topological subroutine needs to be developed to allow series and parallel grouping of coils in order to achieve self-consistent coil and power supply characterization.

3) System thermal models: The present version of SOLXPT3D includes thermal hydraulic and 3D thermal diffusion through a winding pack. However, it does not yet include heat transfer from one winding pack to another. Also, it includes heating of passive structures by eddy currents, but does not model temperature changes in the passive structures. This is particularly important, when cold structure outside the winding pack includes a continuous eddy current loop.

4) Sub-turn heater elements: Quench and finite-N heating can be modeled 'node-to-node', irrespective of turn length, but all pulsed loads are applied to individual turns, since the field of a solenoid is approximately uniform along an entire turn. Sub-turn heater elements are useful to model joints, the possibility of quench initiating from joints, and the dump temperatures due to such joint quenches. Sub-turn heater elements are also needed to do stability analyses, such as the energy margin vs. applied energy, length, and time. Modeling of external heater elements is needed for inductive or resistive elements used to deliberately quench a coil, either for testing stability margin or for inducing nearly uniform quenches in an internal dump to limit local hot spot temperatures.

5) Non-solenoid magnets: These are now treated exclusively by ANSYS, except for the highly idealized assumption of a 1 ½ D single channel model. Because of the difficulties in generalizing non-solenoidal models, this has not been a high priority. MASADA can be used for conceptual design of many types of non-solenoidal systems, but it cannot be used for transient simulations.

6.3 Achievements in FY08

Three main improvements were proposed for FY08. Two of them have been achieved. A more elegant approach, developed this year, should make the third unnecessary. The work in FY08 included the following tasks.

6.3.1 Generalization of the flow paths and thermal integration

Because of a several year commitment to modeling the ITER CS coils, full 3D simulation in SOLXPT3D-Q2 only supported single pancake flow. In order to support the general case of any possible flow path, the hydraulic model was upgraded this year to include multiple pancake and layer flows[30]. Temperature and voltage distributions, due to a quench in the inner coil of a layer-wound, potted, multicoil solenoid system is shown in Figs. 2a, 2b. The code revealed a surprising result that split external coils caused a high enough field gradient, which led to a short initial quench zone. This, in turn, caused high hot spot temperature peaking in two locations, as shown in Fig. 6.2a.

The MIT FY08 proposal to include modeling of multiple in-hand winding, however, was not implemented this year, when it was found that the effort would exceed the value of being able to model a comparatively rare design option. In the case of ITER, this would allow self-consistent simulation of the PF system, as well as the CS, but no other multiple-hand windings are planned.

[30] MAGNETBASE-MIT-FENG-040408-01, Jun Feng, " Solxpt3d-Q2 with addition of universal winding pattern," April 4, 2008

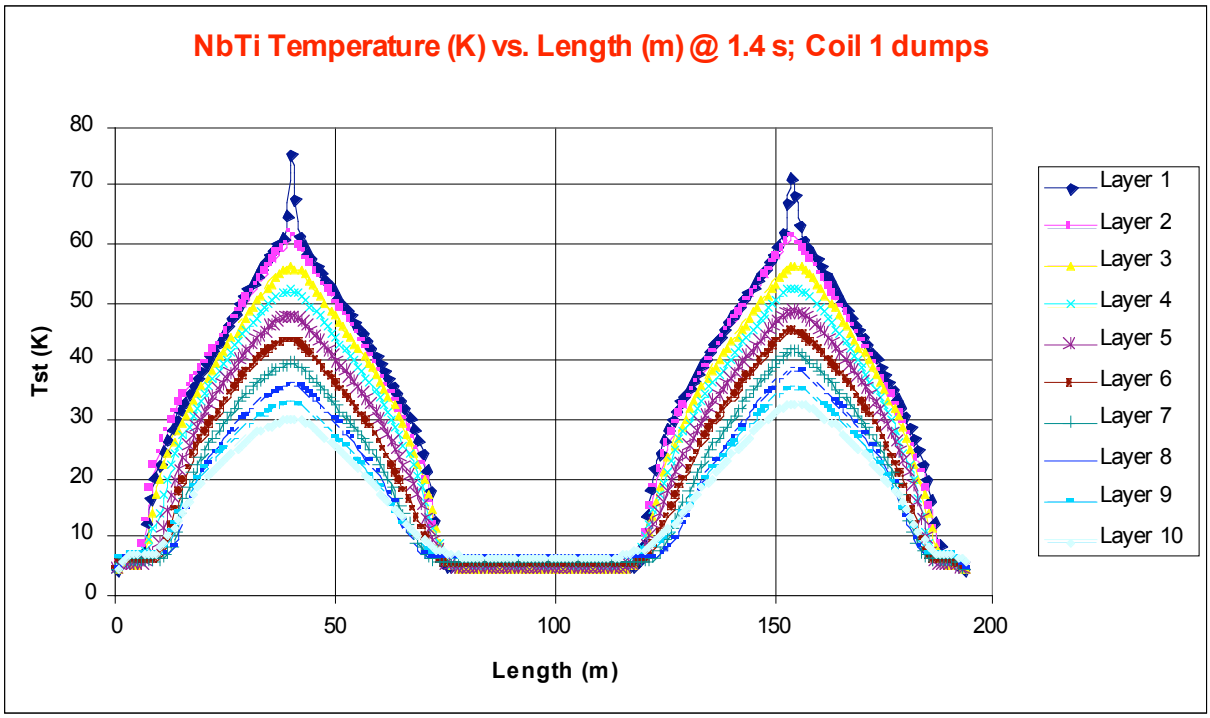

Fig. 6.2a: Superconductor Temperature (K) vs. Length (m); all 10 layers of a potted coil, 1.4 s after the beginning of quench /dump in layer wound solenoid

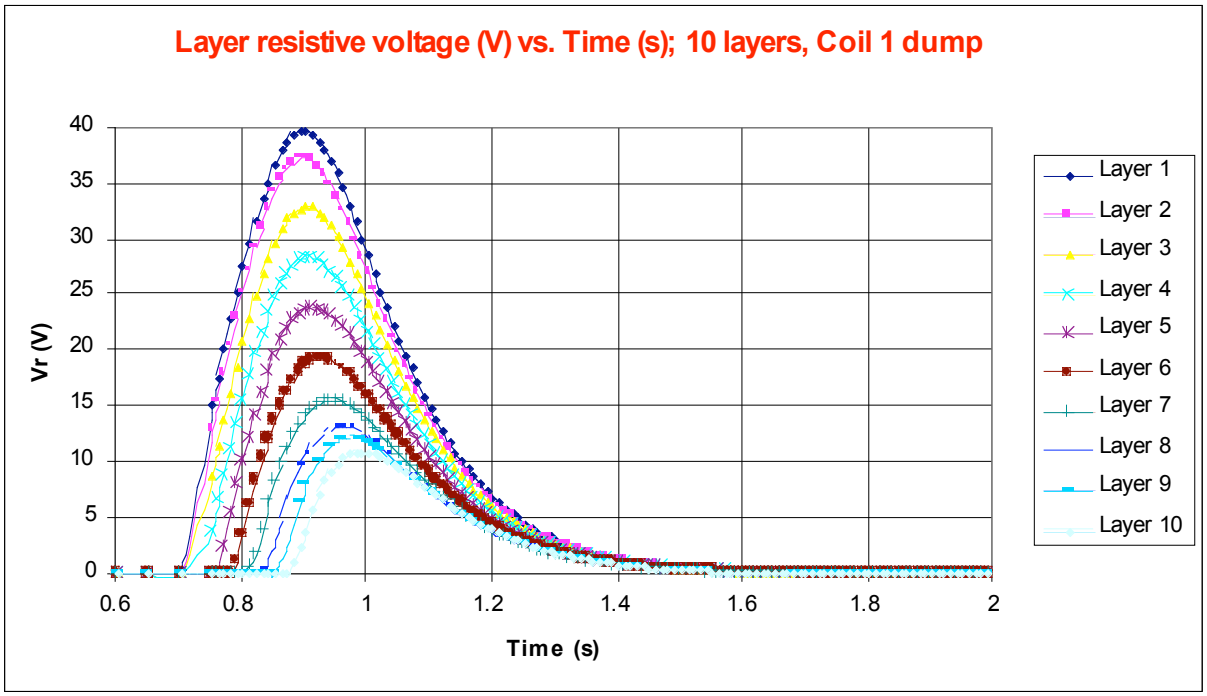

Fig. 6.2b: Internal dump, layer resistive voltage (V), each of 10 layers

Another planned upgrade in self-consistent modeling was to include the inlet and outlet pressure drops between the header and coil channel[31]. This task was completed, but the upgrade was less successful than the generalization to multiple pancake and layer channels, because of two factors. There was a much higher than expected variability in the experimental literature[32], leading to a requirement of a multiplicative factor with intrinsic error bars comparable to simple neglect of these pressure drops. The upgrade made the time steps needed for numerical stability an order of magnitude smaller. It was therefore decided not to include inlet-outlet modeling as a default feature of SOLXPT3D-Q2 in the immediate future.

6.3.2 Upgrade output files for ANSYS

In FY08, SOLXPT3D-Q2 added three-dimensional temperature data to its output files that now allow direct input to ANSYS for thermal stress analysis. Furthermore, the files have been successfully integrated with a self-consistent stress analysis at varying key time points in which the effects of Lorentz loads, precompression, thermal contraction and 3D temperature distributions can be analyzed. It has been discovered in the analysis of non-fusion, potted magnets that the ITER design rule of keeping hot spot temperatures in the internal structure below 150 K does not guarantee structural integrity. Permanent and unacceptably high deformations, including unacceptable field errors, are found to be a frequent consequence of 150 K quenches. It had been at least a decade since there had been any investigation of the consequences of thermal deflections on the ITER magnets and the studies cannot be done routinely with existing tools.

The stress distribution has now been calculated for a quench dump in the ITER CS1U coil at several key time points, during and following a vertical disruption[33], as shown in Figs. 6.3a, and 3b. The 3D quench analysis also includes the 3D time history of the helium pressure.

[31] MAGNETBASE-MIT-FENG-052408-01, Jun Feng, "Rev1: Modified code to include the singular pressure drop at inlet/outlet," May 24, 2008

[32] ITER-EFDA-CEA, 31/01/2005, S. Nicollet, "REVIEW OF PRESSURE DROP FOR ITER COILS," CEA MEETING ON THE ITER CRYOGENIC SYSTEM (6th), CEA-Grenoble, Jan 31-Feb 1, 2005

[33] MAGNETBASE-MIT-TITUS-041608, Peter Titus, "Calibration and Setup of First Structural Interpretation of Feng Quench Simulation ," April 16, 2008; MAGNETBASE-MIT-PTitus-061008, Peter Titus, "First Structural Interpretation of Feng Quench Simulation," June 10 2008

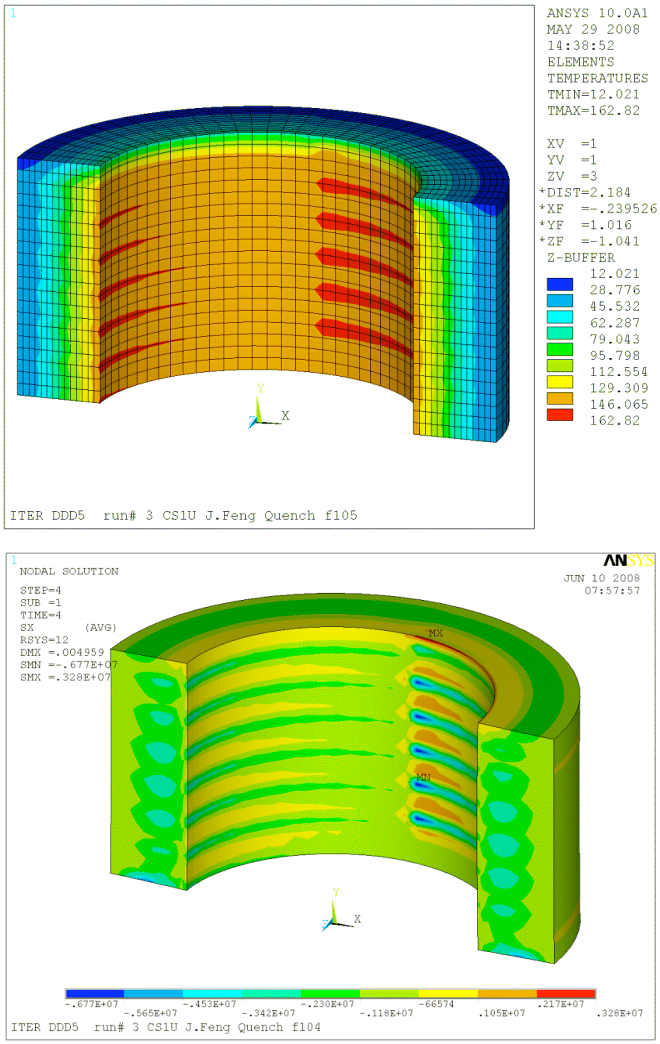

Fig. 6.3, a): Temperature distribution in ITER CS1U, 8 seconds after beginning of quench at 530 s (EOB), peak temperature exceeds 150 K allowable, b): Radial stress in CS1U at 538 s, peak tension of 3.3 MPa not allowed, but small fraction of tension due to Hoop loads.

It was discovered that the local hot spot temperatures exceeded the ITER allowable of 150 MPa with a peak conduit temperature of 170 K (162 K is shown in Fig. 6.3a, at 538 s, i.e. 8 s after the beginning of a disruption at EOB). However, the structural analysis did not indicate failure. The worst stress calculated, shown in Fig. 3b was 3.3 MPa radial tension in the insulation. While tension in the insulation undesirable, this is smaller than the peak radial tension due to Lorentz loads. This is the first direct application of a magnet quench model to a finite element stress calculation in the history of the US fusion program.

6.3.3 Increased dimension to allow winding pack 'splitting' in initial conditions

The third planned upgrade was to change superconductor properties in an individual coil from scalars to vectors. The purpose was to allow self-consistent modeling of either graded

windings or of thermal communication between modules, and also to permit self-consistent modeling of energy margins in realistic situations, such as having a damaged length of conductor. It would allow forcing quenches that begin in low field regions, a case that is less probable than high field, but more dangerous to coil protection, when it occurs, and would also be used to simulate quenches that originate at joints – an event that is both probable and dangerous.

This upgrade was cancelled, when it was realized that all properties could remain scalars and that heating in specific locations could be implemented entirely through the input file. This can be done simply by introducing a new 'pulsed loss' mechanism, similar to hysteresis, coupling, eddy current, and Finite-N heating. The heater element could be specified by five parameters in the input file: power/length, length, position, time duration, and starting time. The loss could then be superimposed with other losses through a call to the ACLOSS subroutine. This will require orders of magnitude less new coding than changing the dimensionality of a large number of key parameters and is less likely to introduce bugs into the code. It will not, however, allow modeling of grading, which will require a second upgrade to allow heat transfer between modules, considering each grade as separate, seriesed coils.

6.4 Work Plan

The long-term upgrade plan is described in the Program Goals section, 6.2. The development plan for FY09 includes the following upgrades, calibration and design exercises.

1) HTS Model: At least one model for high-temperature superconductor tapes will be developed, beginning with advanced YBCO. This will be applied to a DEMO scale design, based on ARIES-AT, and calibrated against the insert coil, built by Superpower for the 26.8 T National High Magnetic Field Laboratory NMR magnet. A model in which both critical current and hysteresis loss is a function of both field and temperature will be based on information provided at MIT's visit to Superpower in FY08 and shown in Fig. 6.4.

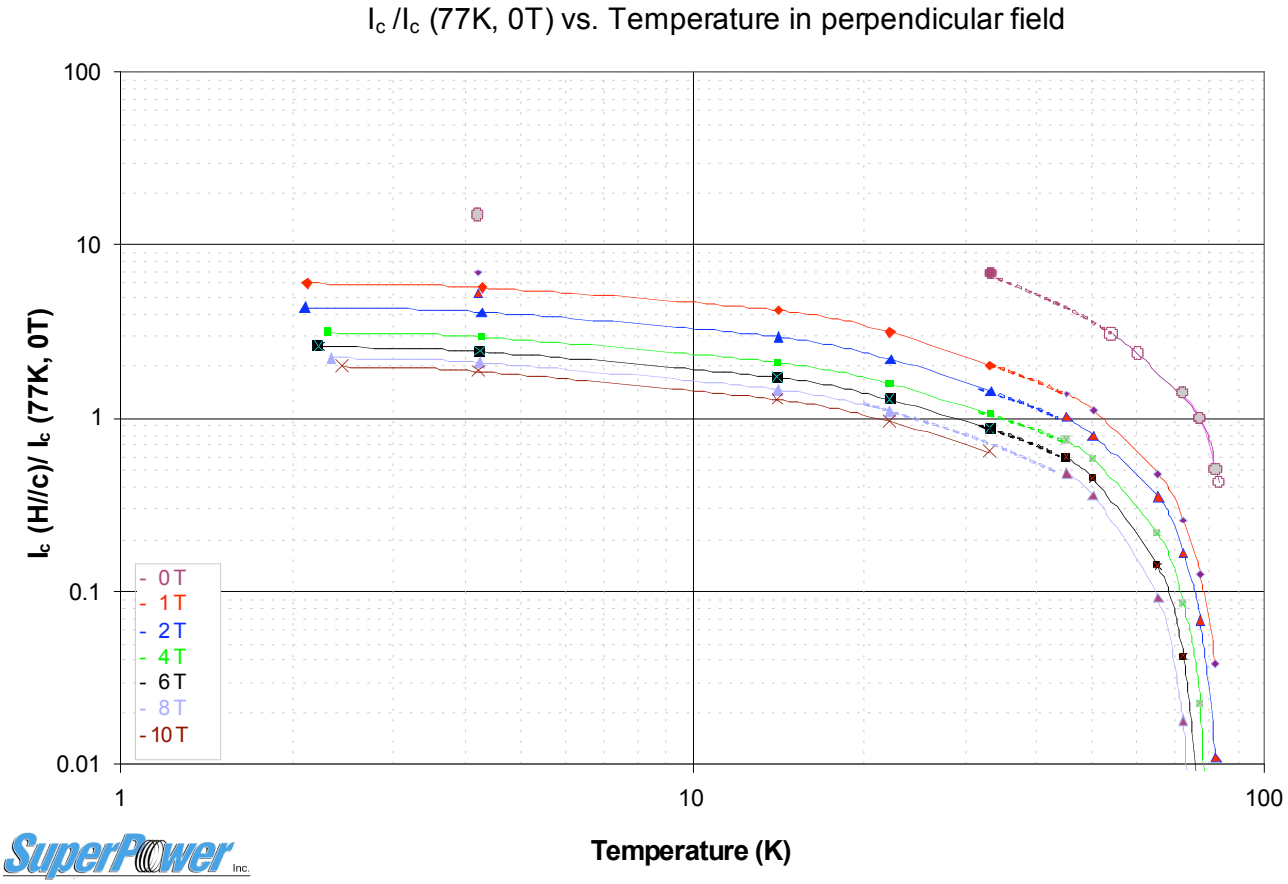

Fig. 6.4: Superpower-provided curve of state-of-the-art YBCO tape performance

2) Upgraded circuit topology model. The next step towards a fully-general, "SPICE-like" circuit model will be to allow placing any of the four existing circuit modes, i.e. current, voltage, resistor, and voltage + resistor sources, in series with each other. A fifth circuit mode, cold diode, will also be added to the model. This will cover the key circuit design features of most practical superconducting magnet power supplies.

3) Heat-transfer between modules. The heat coupling module and input file will be upgraded to allow heat transfer between adjacent superconducting modules and between superconducting modules and passive cold structure. The addition of specific heat models for all practical materials, e.g. steel, aluminum, titanium, will not be included in the FY09 work plan. This should allow, however, the modeling of the important feature of a quench spreading from one winding to another.

4) Arbitrary length heating source. This upgrade, discussed above, adds an input-defined heating source to the pulsed loss terms accumulated in the ACLOSS module. This will allow the simulation of quenches that originate at a joint and internal quench protection, using

resistive heaters. It will also permit parametric studies of energy margin as a function of power, time, and length.

7 SUBTASK-6 VLT ENABLING TECHNOLOGY MAGNETS PROGRAM LEADERSHIP

Since many years the Office of Fusion Energy Sciences has organized all enabling technology activities under a national structure called the Virtual Laboratory for Technology. Within that program Joseph Minervini has served as spokesperson for Magnet Technology since 1996. In that role, he interacts with the VLT leadership and responds to OFES request for programmatic guidance and input and annual budget requests. Also, in general, MIT serves as a national resource to the OFES program for support and guidance of SBIR programs and as a source of expert support for magnet engineering technology of various national fusion projects. MIT has also served the national program as a partner in bilateral and multilateral international projects and technology exchanges. MIT is eager to continue offering its support to the national fusion program and to the US contributions to international collaborations during the new cooperative agreement duration.

We note that any substantial joint superconductor or magnet technology collaborative development project, whether national or international, would require funding in addition to the modest base program proposed here.